INVESTIGATION OF NANOSTRUCTURED ELECTROCATALYSTS AND MASS TRANSPORT PHENOMENA IN POLYMER ELECTROLYTE FUEL CELLS

by

GABRIEL A. GOENAGA

A dissertation submitted to the Graduate Faculty in Physics in partial fulfillment of the requirements for the degree of Doctor of Philosophy, The City University of New York

2010

This manuscript has been read and accepted for the
Graduate Faculty in Physics in satisfaction of the
dissertation requirement for the degree of Doctor of Philosophy.

Steven G. Greenbaum

Date — Chair of Examining Committee

Steven G. Greenbaum

Date — Executive Officer

Di-Jia Liu

Hector Jiménez

Neepa Maitra

Yuhang Ren

Supervisory Committee

THE CITY UNIVERSITY OF NEW YORK

Abstract

INVESTIGATION OF NANOSTRUCTURED ELECTROCATALYSTS AND MASS TRANSPORT PHENOMENA IN POLYMER ELECTROLYTE FUEL CELLS

by

Gabriel A. Goenaga

Adviser: Professor Steven Greenbaum

Proton exchange membrane (PEM) fuel cells (FC) are promising devices in the search of clean and efficient technologies to reduce the use of fossil fuels. However, their poor performance in dynamic applications and high cost of platinum group metal (PGM) catalysts, have prevented them from becoming an affordable solution. This dissertation comprehend three research projects that study the mass transport phenomena in modified PEMs, the reduction of the amount of PGM catalyst used for oxygen reduction reaction (ORR) and the use of non-PGM catalysts as alternative catalyst to Pt for ORR.

Nafion is the most used PEM for FC applications. Nafion proton conductivity is proportional to its degree of hydration, what imposes low temperature operation to maintain appropriate water content. In this research, Nafion composite membranes doped with hydrophilic metal inorganic particles have been studied using pulse field gradient (PFG) nuclear magnetic resonance (NMR). The Nafion

composite membranes were found to have higher water uptake, higher water retention, higher water diffusion and, in some cases, lower methanol diffusion (crossover) than the filler free Nafion membrane.

The amount of Pt and PGM catalysts supported on carbon used in the electrodes, has a great impact in the PEMFC cost. In particular, it is of high relevance to reduce the amount of Pt in the cathode electrode, in which the sluggish ORR demands four to five times more Pt catalyst than in the anode. In this thesis is shown that the use of aligned carbon nanotubes (ACNTs) as Pt support, allows a more uniform distribution of the Pt nanoparticles, what in addition to their high hydrophobicity and high corrosive resistance, lead to improved mass transport and stability of the membrane electrode assembly (MEA), when compared to a benchmark MEA that uses Pt catalyst supported on carbon black. The improvement was accomplished using less Pt than in the benchmark MEA.

Replacing Pt with non-PGM catalyst can lead to an affordable PEMFC. However, finding a non-PGM catalyst with similar ORR performance than Pt has been a challenge for over two decades. In the present work, two novel Co-based non-PGM catalysts have been studied, showing promising preliminary results. Both are 3-D structured materials, a Co containing porous conjugated polymer and a Co imidazolate metal organic framework (MOF). Rotating disk and rotating ring disk electrode experiments show that both materials, present ORR catalytic activity compared to state of the art non-PGM catalyst. A major advantage of

this approach is that the 3-D structure can be used as a template for different transition metals or metal alloys (Fe, Ni, Ta) that can potentially be used to improve the ORR catalytic activity.

To my father's memory, my motivation to pursue all my academic goals. To my mother, for her unconditional support and patience. To my sisters Eloina and Orisnella, to my brothers Miguel and Jose, and to my nieces and nephews.

Acknowledgements

I would like to thank Professor Steven Greenbaum and Dr. Di-Jia Liu for giving me the opportunity of pursuing my Ph.D. under their guidance.

I also would like to thank Dr. Romesh Kumar, Dr. Debbie Myers, Dr. Nancy Kariuki, Dr. Xiaoping Wang, Dr. Shengqian Ma, Dr. Shengwen Yuan, Dr. Suhas Niyogui, Dr. Yunbing Yang from Argonne National Laboratory, and Dr. Phil Stallworth from Hunter College for useful discussions and advice during my research.

To my friends Nestor, Armando, Tatiana, Carlos, Alex, Amish, Luz, Lina, Kodi, Jaime, George, Nicole, Arun, Allida, Jacky, Vilma, Jessica, Demetra, Sai, Neng and Weiling for all their support and company during this journey.

Table Of Contents

List Of Figures

List Of Tables

1. Experimental Techniques for Fuel Cell Characterization

1.1. Introduction

The necessity of reducing the dependence on non-renewable energy, such as fossil fuels, and increasing environmental consciousness have recently drawn great interest in alternative energy sources. Among these alternative sources can be mentioned wind, solar, biomass and geothermal. For portable applications rechargeable batteries and fuel cells are the preferred devices. Fuel cells (FC) are an excellent option because they can produce electric energy with high efficiency and in a very clean manner. For instance, when hydrogen is used as the fuel, the only byproducts are water and heat. FC can also be “re-fueled” in short time, what make them ideal for long term running applications.

The FC technology has been around since 1839, when its functioning principle was discovered. However, it was forgotten for a long time because of its low efficiency and practical problems. The ideal FC is a device that converts chemical energy into electrical power in an efficient way, and the byproducts are water and heat only. This a very clean manner to produce electricity, compared to a combustion engine. A FC consists of two electrodes – the anode and the cathode – separated by a proton conducting membrane. Pure hydrogen is fed to the anode and oxygen or air to the cathode. A catalyst in the anode dissociates the hydrogen into free protons and electrons. The free electrons are forced to flow toward the cathode through an external circuit that uses them as

an electrical current. At the same time, the protons go to the cathode through the membrane; at the cathode they recombine with the electrons and oxygen to form water and heat. The overall reaction is:

$$2H_2(gas) + O_2(gas) \rightarrow 2H_2O + Energy \qquad (1.1)$$

Recent advances in the fuel cell field have led to the development of cells with efficiencies within 30% to 40% compared to 10% to 20% efficiency of the combustion engine.

In order to operate a FC extremely high pure hydrogen is required, typically CO concentrations of less than 10 ppm are desirable. The voltage produced by a fuel cell is limited by the reactants supplied to the cell, and its theoretical maximum is 1.23V at room temperature. The typical values in a real FC are around 0.7 V. The current produced by the cell is directly proportional to its cross-sectional area. To produce higher voltages, the individual cells are connected in series forming a stack [1].

The hydrogen can be obtained from water by means of electrolysis or extracted from fossil fuels as natural gas, gasoline, propane, etc, using a reformer. The reformer is a device that dissociates the fuel molecules to obtain high purity hydrogen, which is fed to the cell. Obtaining hydrogen from electrolysis is an expensive and inefficient procedure, but future advances in fuel cell technology will certainly produce corresponding improvements in electrolyzers. At present, more energy is spent to separate water into hydrogen and oxygen than the

usable energy obtained when the hydrogen and oxygen are combined in a fuel cell. On the other hand, the fuels used to supply the energy for the electrolysis process produce pollutants, except for the wind mills or solar panels, which are both expensive technologies. Another problem with hydrogen gas is that it is hard to compress and store, which limits its applications. Direct methanol fuel cells (DMFC) invented by the Jet Propulsion Laboratory (JPL), use methanol as fuel and do not need a reformer to produce the hydrogen. In addition, liquid methanol is easy to store, and is obtained from many different natural sources as corn, sugar cane, etc. that make it cheap. However, the DMFC is a technology in development that presents some problems that make it inefficient compared to other fuel cells in the market.

According to the material used for the membrane FCs are classified as Alkaline fuel cells (AFC), solid oxide fuel cells (SOFC), phosphoric acid fuel cells (PAFC), molten carbonate fuel cells (MCFC) and polymer electrolyte membrane fuel cells (PEMFC). Figure 1.1. shows a schematic of a PEMFC.

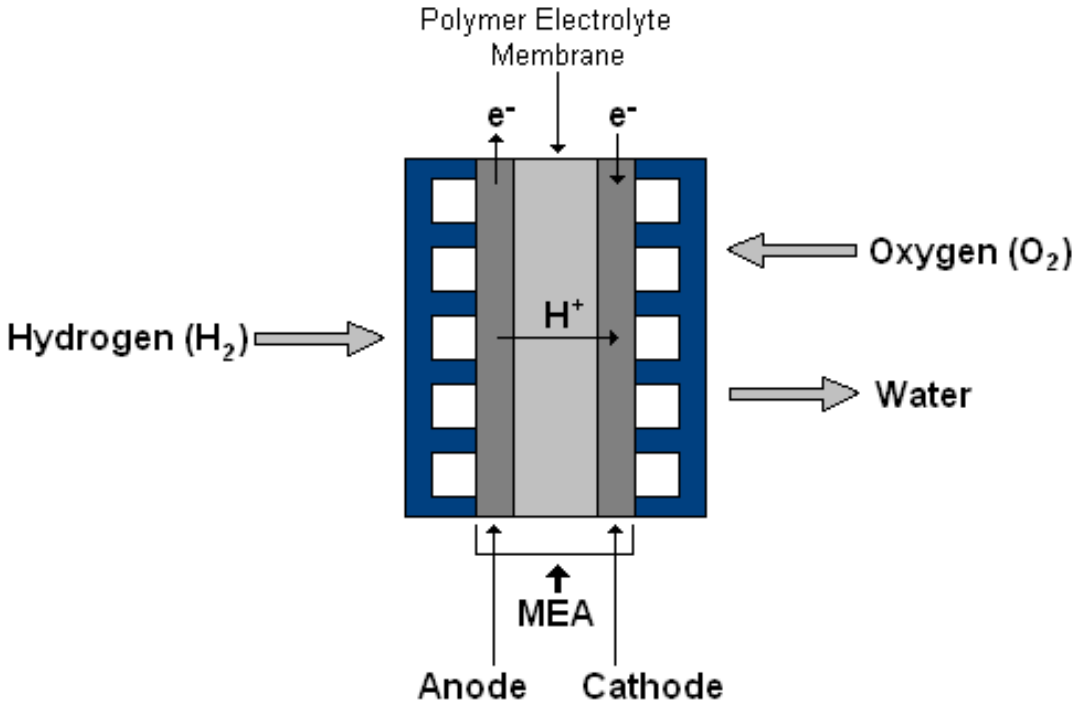

Figure 1.1. PEMFC components and functioning.

The desirable characteristics of a good PEM are high ionic conductivity, very low electronic conductivity, low fuel and oxidant permeability, thermal and oxidative stability and low cost. Nafion® invented by DuPont is the most common used material for PEMFC applications. Chapter 2 presents a variable pressure and variable temperature nuclear magnetic resonance characterization of Nafion membranes doped with inorganic materials particles, showing improvement in water retention at high temperatures, diffusion and, cross over reduction when compared to pure Nafion.

The operation temperature of PEMFC is about 80 ^{o}C. This low operation temperature makes them suitable for various types of applications, including

vehicles, stationary and portable devices. However, this also imposes the need of a catalyst to facilitate the hydrogen oxidation and oxygen reduction in the cell's electrodes. At present the state of the art catalyst for these reactions are Pt group metals (PGM) with limited natural reserves and prohibitive cost, what has created a major barrier for large scale commercialization of PEMFCs. The oxygen reduction reaction (ORR) at the cathode of a PEMFC represents a very important electrocatalytic reaction, and is of major interest because its low speed demands four to five times more Pt catalyst than the anode [1].

Intensive efforts have been devoted to reduce the amount of Pt used in the cathode, as well as to search for non-PGM materials with ORR catalytic activity as a Pt alternative. In this research both approaches have been addressed. Chapter 3 describes the use of aligned carbon nanotubes as Pt catalyst support, for the cathode electrode in a membrane electrode assembly. Single cell characterization shows better fuel cell performance reducing the amount of Pt catalyst used can be accomplished. Chapter 4 describes the synthesis and electrocatalytic characterization of two novel non-PGM catalyst materials, with promising ORR catalytic activity as cathode catalyst materials.

1.2. Nuclear Magnetic Resonance Technique

Nuclear magnetic resonance (NMR) is a technique that exploits the magnetic properties of nuclei to study the molecular structure and dynamic processes of a

sample. NMR is possible because certain nuclei posses magnetic moments and angular momenta.

When an external magnetic field of intensity B_o is applied to a sample, the nuclei will tend to align along the field, in order to minimize the magnetic energy. Electrons and nuclei in an atom possess intrinsic magnetism (magnetic moment) and spin angular momentum. This magnetism is permanent. The magnetic moment and the spin are related by:

$$\mu = \gamma S \qquad (1.2)$$

where γ is the gyromagnetic ratio.

The angular momentum of a particle with spin is a vector that can be oriented in any direction in space. In the absence of an external magnetic field the distribution of the magnetic moments in a material is isotropic and the total magnetization is close to zero. If a magnetic field is applied, the spin magnetic moments start precessing in a cone around the orientation of the external field. This precession makes a cone of constant angle between the spin magnetic moment and the magnetic field.

The frequency of this precession is called Larmor frequency. It is proportional to and uniquely determined by the gyromagnetic ratio γ and the strength of the magnetic field B_o. The Larmor frequency is defined by:

$$\omega_0 = -\gamma B_0 \qquad (1.3)$$

The sign of ω_0 indicates in what sense the spin is precessing (clockwise or counterclockwise). In a given magnetic field the precession frequency ω_0 is different for every nucleus because each has a uniquely defined γ. The figure 1.2 shows a drawing of this.

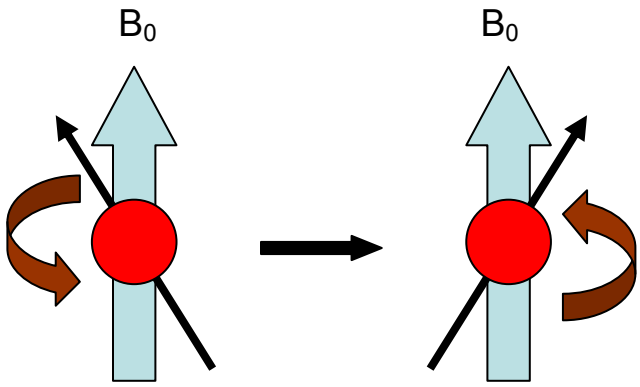

Figure 1.2. Spin precession around a constant magnetic field.

The spin angular momentum of a nucleus placed in a static magnetic field in the z direction, will orientate such that its z component is given by

$$S_z = m\hbar \qquad (1.4)$$

where m can take the values m = I, I -1, …, -I. There are (2I+1) possible orientations (also called nuclear Zeeman levels) of the spin angular momentum and the magnetic moment in the magnetic field. For protons and ^{13}C, for example, which have I = ½ there are two possible orientations + ½ and – ½.

The magnetic moment along the z direction is

$$\mu_z = m\gamma\hbar \qquad (1.5)$$

The energy of the magnetic dipole in a magnetic field of intensity B_0 is

$$E = -\mu_z B_0 = -m\gamma\hbar B_0 \qquad (1.6)$$

For protons or ^{13}C there are two values of the energy corresponding to m = + ½ and m = – ½. If m = + ½, μ_z is parallel to the magnetic field, which is the lower energy state, for m = – ½, μ_z is antiparallel to the field, which gives the higher energy state. The first state is described by the spin function α and the latter by the spin function β. The figure 2 shows the energy levels in the presence of magnetic field for a nucleus with I = ½.

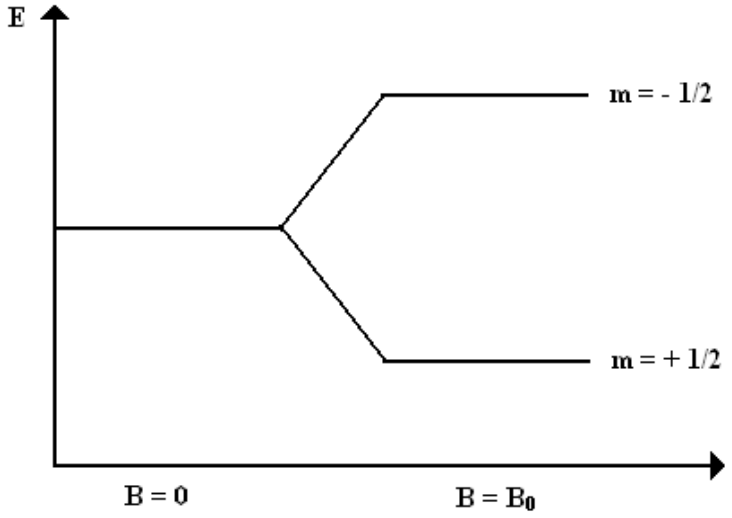

Figure 1.3. Energy level splitting in the presence of a magnetic field.

The energy difference between two adjacent energy levels is

$$\Delta E = \gamma\hbar B_0 \qquad (1.7)$$

In thermal equilibrium, the nuclei in a macroscopic sample distribute between the energy levels according to Boltzmann statistic. For nuclei with I = ½

$$\frac{N_\beta}{N_\alpha} = e^{-\frac{\Delta E}{k_B T}} \approx 1 - \frac{\Delta E}{k_B T} = 1 - \frac{\gamma \hbar B_0}{k_B T} \qquad (1.8)$$

where N_β is the number of nuclei in the highest energy level, N_α is the number of nuclei in the lowest energy level and k_B is the Boltzmann constant. For protons ΔE is very small compared to $k_B T$ that N_β and N_α have approximately the same value. N_α exceeds N_β in the range of parts per million (ppm).

If the z components of all the nuclear magnetic moments in a sample are added, there will be a net macroscopic magnetization M_0 along the field direction, because N_α is greater than N_β. It is possible to induce a transition of nuclei from a lower to a higher energy level, irradiating them with an radio frequency (rf) pulse of frequency equal to the Larmor frequency. Transitions between levels only occur at this frequency and are only possible between adjacent levels of energy, i.e. when $\Delta m = \pm 1$.

When the rf pulse is applied to a coil, it generates a magnetic field of intensity B_1 perpendicular to the static field B_0. The individual nuclear moments will flip due to the new magnetic field and the total magnetization M_0 is rotated away from the static field too. After the magnetic field is turned off, the magnetization precesses freely and decays.

If enough energy is put into the system, it is possible to make the net magnetization along the z axis, M_z equal to zero. This can be done applying a

90^o pulse along the x axis or $\frac{\pi}{2}_x$ pulse. The time constant which describes how M_z returns to its equilibrium value is called the spin lattice relaxation time T_1. The expression for M_z in terms of time is:

$$M_z = M_0\left(1 - e^{-\frac{t}{T_1}}\right) \qquad (1.9)$$

When the 90^o pulse is turned off, the spins resume their precessional motion, and the net magnetization precesses too. The macroscopic nuclear magnetization rotates in the x-y plane, perpendicular to the magnetic field. The precession of the transverse magnetization is equal to the Larmor frequency. The magnetization components after a time t have the form

$$M_y = -M_0 \cos(\omega_0 t) e^{-\frac{t}{T_2}} \qquad (1.10)$$

$$M_x = -M_0 \sin(\omega_0 t) e^{-\frac{t}{T_2}} \qquad (1.11)$$

The transverse magnetic moment precesses at the Larmor frequency and decays at the same time. The time constant T_2 is called the spin spin relaxation time [2-4].

1.2.1. Diffusion

The NMR parameters spin lattice relaxation time T_1, spin spin relaxation time T_2, line width, spectral pattern are sensitive to the molecular motions. Measurements of the translational or self diffusion coefficient are important to

determine sizes and shapes of molecules or other factors related to their transport properties such as local viscosity. The pulsed gradient spin echo NMR method is used to measure the self diffusion coefficient D.

For macromolecules the relation between D and the molecular size is usually given by the Stokes'-Einstein equation

$$D = \frac{k_B T}{f} \qquad (1.12)$$

where f is the friction factor. For a spherical particle with hydrodynamic radius R_h immersed in a fluid of viscosity η, Stokes' law gives $f = 6\pi\eta R_h$.

The pulsed field gradient (PFG) NMR experiment for diffusion measurements permits variation of the gradient areas without changing the echo time, so that the attenuation resulting from relaxation can be held constant; also the echo can be recorded in homogeneous magnetic field, in consequence the spectral information is kept and frequency resolved diffusion measurements are possible. To apply these gradients, current pulses are required and this produces heat, mechanical forces and eddy currents. The NMR pulse sequence used is shown in figure 1.4. Previous to this experiment it is necessary to obtain the value of the time constant T_2.

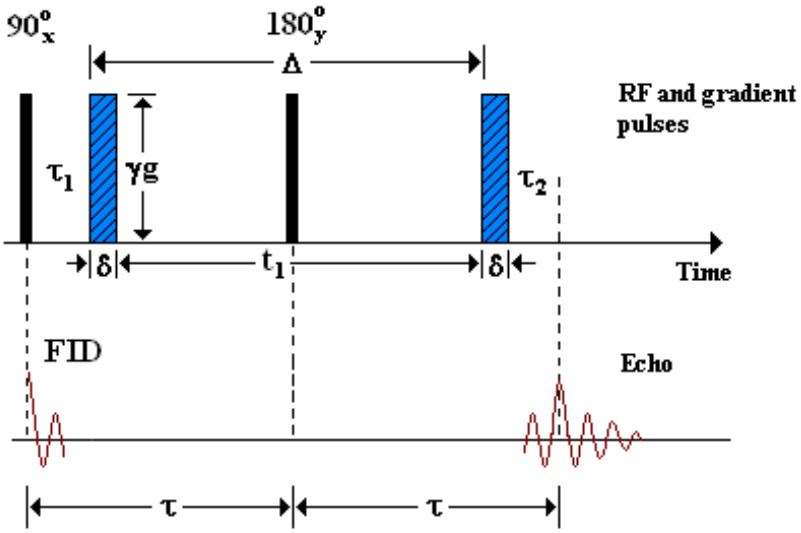

Figure 1.4. Pulsed field gradient sequence used in Diffusion NMR measurements.

The echo attenuation resulting from diffusion for the sequence shown in figure 1.4 is:

$$S(2\tau) = M_0 \exp(-2\tau / T_2)\exp(\left(-Dq^2(\Delta - \delta/3)\right) \qquad (1.13)$$

where q = γgδ. From this equation the value of D can be obtained [5].

1.3. Rotating disk electrode and rotating ring disk electrode experiments

The investigation of the oxygen reduction reaction (ORR) electrocatalysts for FC applications normally implies studying several catalyst samples. The process of testing every possible catalyst candidate in a single cell is tedious, expensive and in a certain way unnecessary. Instead, a prescreening method can be used to determine which catalyst materials are good candidates, and worth testing in the actual cell. Rotating disk electrode (RDE) and rotating ring disk electrode

(RRDE) experiments allows determining the ORR kinetics (how fast the reaction take place) and the amount of peroxide produced during the reaction (number of electrons transferred).

The RDE consists of a glassy carbon (GC) disk embedded in an inert insulating material (Teflon), mounted in a rigid shaft. GC is used because carbon is electrochemically inert over the range of the electrode potentials relevant to ORR studies. The RDE experiment helps to determine how fast oxygen reaches the GC electrode (mass transfer), and how fast oxygen is reduced at the electrode (reaction kinetics). In the RRDE a ring electrode (typically gold or platinum) is placed around the GC disk, separated from it by a thin Teflon insulating gap. The disk and the ring have the same axis of rotation. The ring is used to detect the amount of peroxide produced at the disk after the ORR has taken place. Figure 1.5 show pictures of actual RDE and RRDE electrodes.

(a) (b)

Figure 1.5. RDE and RRDE electrodes. (a) GC RDE electrode, (b) GC/Pt RRDE electrode configuration.

For these experiments, a thin layer of the catalyst, in the form of an ink, is deposited on the GC disk. The solution flow pattern induced by the electrode rotation continually draws fresh electrolyte solution, containing dissolved oxygen, towards the center of the GC disk. Oxygen is reduced when reaches the catalyst coated electrode surface. Figure 1.6 shows the RDE experimental setup.

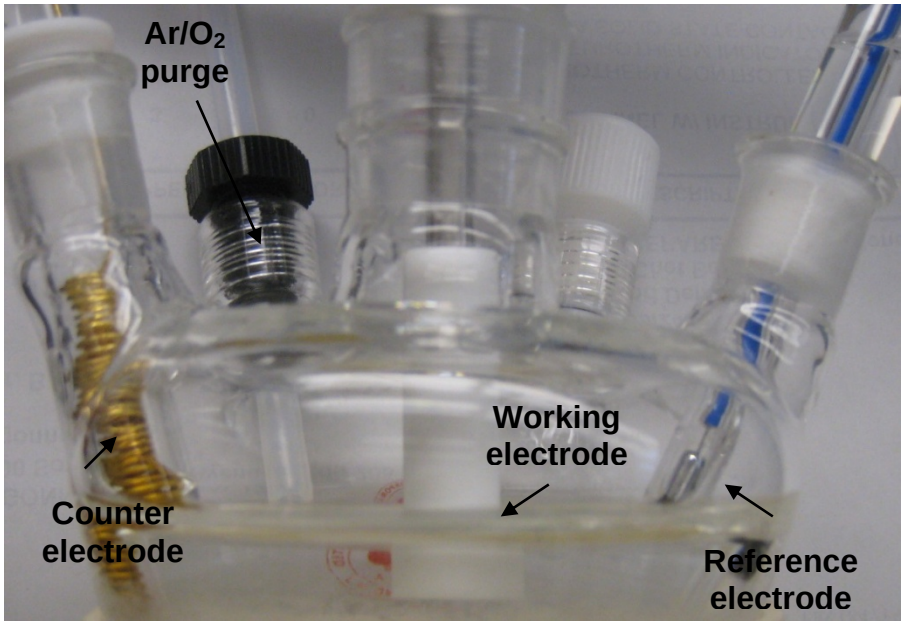

Figure 1.6. RDE experimental setup.

The mass transport of oxygen increases as the rotation speed increases, due to more oxygen can reach the electrode. At high enough rotation speed, the rate at which oxygen arrives at the electrode surface approaches the rate at which the electrocatalyst reduces oxygen. The current measured at this point (limiting current) is governed by the kinetic properties of the catalyst. The Koutecky-Levich equation (equation 1.14) gives the relationship between the limiting

current density *j*, the kinetic current density j_k and the rotation speed ω. The kinetic current represents the current in the absence of any mass-transfer effects.

$$\frac{1}{j} = \frac{1}{j_k} + \frac{1}{0.62nFD_{O2}^{2/3}\nu^{-1/6}C_{O2}\omega^{1/2}} \qquad (1.14)$$

Where *n* is number of electrons transferred, *F* the Faraday's constant, D_{O2} the diffusion coefficient of O_2, *v* = kinematics viscosity of the electrolyte and C_{O2} the O_2 concentration in the electrolyte.

The reduction of oxygen at the catalyst coated electrode produces water or peroxide, depending on whether the catalyst favors the 4 or 2 electron transfer mechanism, respectively. For FC applications, the 4 electron transfer mechanism is desired because peroxide production is detrimental for the Nafion PEM [6,7].

The number of electrons transferred can be calculated from the slope of the Koutecky-Levich plots (*1/j* vs. $\omega^{-1/2}$) if the catalyst reaches the limiting current, the area of the GC covered by the catalyst, D_O, C_O and *v* are known [8]. However, for certain catalyst the electrode coverage is not complete and/or limiting current is not reached. In this case the RRDE technique becomes a very powerful and convenient tool to determine the number of electrons transferred during ORR. The rotation flow pattern pushes away the ORR products in an outward radial direction, and can be detected at the ring electrode surrounding the GC

electrode. The numbers of electrons transferred (*n*) can be determined from the relationship between the current generated at the disk (I_d) when oxygen is reduced and the current generated at the ring (I_r) when peroxide is detected. The expression for the number of electrons transferred is given in equation (1.15)

$$n = \frac{4I_d}{I_d + I_r/N} \qquad (1.15)$$

Where *N*, the collection efficiency, is the fraction of the ORR product generated at the disk electrode that can be detected at the ring electrode. The value of N depends only on the dimensions of the ring and disk electrodes and is defined as [9,10],

$$N = -I_r/I_d \qquad (1.16)$$

1.4. Fuel cell polarization curve

The overall fuel cell reaction, given by equation 1.1, is the same as the reaction of hydrogen combustion, with products of water and heat. By definition, the heat of a chemical reaction is the difference between the heat of formation of the products and the reactants:

$$\Delta H = h_f(H_2O) - h_f(H_2) - \tfrac{1}{2} h_f(O_2) \qquad (1.17)$$

The heat of formation of liquid water is -286 kJ/mol and the heat of formation of the constituent elements is zero, then

$$\Delta H = -286\,kJ/mol \qquad (1.18)$$

This hydrogen heating value is a measure of the input energy into the FC, and the portion of this energy that can be converted to electrical energy is given by the Gibbs free energy:

$$\Delta G = \Delta H - T\Delta S \qquad (1.19)$$

where ΔS represents irreversible losses due to creation of entropy by the formation of hydrogen, oxygen, liquid water and water vapor. At 25 ^{o}C, out of 286.02 kJ/mol of available energy, only 237 kJ/mol can be converted into electrical energy.

The electrical work is defined as,

$$W_{el} = qE = nFE \qquad (1.20)$$

with n equal to the number of charges and F is the Faraday constant. In a fuel cell the work is given by the Gibbs free energy (equation 1.19), which equated to (1.20) gives an expression for the fuel cell theoretical voltage at room temperature:

$$E = -\frac{\Delta G}{nF} = 1.23\,V \qquad (1.21)$$

The theoretical fuel cell efficiency is the ratio between the electrical energy produced and the input energy or hydrogen heating value:

$$\eta = {\Delta G}/{\Delta H} = 83\,\% \qquad (1.24)$$

However, even at equilibrium when no load is connected to the FC, the voltage (open circuit potential) for specific conditions of temperature, pressure and reactants concentration, is lower than the theoretical value, normally less than 1 V. This means that there are some losses in the fuel cell even when no external current is being generated. The total FC voltage is given by:

$$E_{cell} = E_{cathode} - E_{anode} \quad (1.25)$$

By definition, at equilibrium the anode voltage is zero and the cathode voltage is E_r = 1.23 V (at 25 ^{o}C).

When a load is connected to the FC, the voltage drops even more as a function of the current being generated. Voltage losses in a FC are caused by the kinetics of the reactions, internal electrical and ionic resistance, difficulty to getting the reactants to reaction sites, internal stray currents and crossover of reactants.

The voltage needed to get the electrochemical reaction going is called the activation polarization, and it is associated with sluggish electrode kinetics. The activation polarization takes place in both, the anode and the cathode. Taking this voltage loss in consideration, the total FC voltage becomes:

$$E_{cell} = E_r - \Delta V_{act,c} - \Delta V_{act,a} = E_r - \frac{RT}{\alpha_c F}\ln\left(\frac{j}{j_{o,c}}\right) - \frac{RT}{\alpha_a F}\ln\left(\frac{j}{j_{o,a}}\right) \qquad (1.26)$$

where j is the total current density, j_o is the current density at equilibrium and α the transfer coefficient. The activation polarization of the hydrogen oxidation is much smaller than activation polarization of the oxygen reduction reaction, and the last term in equation (1.26) can be neglected.

$$E_{cell} = E_r - \frac{RT}{\alpha F}\ln\left(\frac{j}{j_o}\right) \qquad (1.27)$$

In addition, losses due to internal currents and crossover can occur. Hydrogen molecules as well as some electrons can migrate to the cathode through the PEM membrane. For each hydrogen molecule that crossover to the cathode there are two less electrons contributing to the electrical current, these losses become significant at equilibrium and when the cell is operating a low current densities. The total current density is defined by:

$$j = j_{ext} + j_{loss} \qquad (1.28)$$

The cell potential then becomes

$$E_{cell} = E_r - \frac{RT}{\alpha F}\ln\left(\frac{j_{ext} + j_{loss}}{j_o}\right) \qquad (1.29)$$

At open circuit potential no current is being generated, j_{ext} is zero and the cell voltage is defined by:

$$E_{cell} = E_r - \frac{RT}{\alpha F}\ln\left(\frac{j_{loss}}{j_o}\right) \qquad (1.30)$$

Ohmic losses are also present in FC due resistance to the flow of ions throughout the electrolyte, electronic resistance in the FC cell components and in the electrical contacts, the sum of these resistances is called the internal resistance R_i. These losses follow Ohm's law.

$$\Delta V = jR_i \qquad (1.31)$$

Finally, concentration polarization losses occur when a reactant is consumed rapidly at the electrode by the electrochemical reaction. The reactant concentration at the catalyst surface depends inversely on the current density, and is zero when the rate of consumption exceeds the diffusion rate. The current density at which this happens is called the limiting current density. A fuel cell cannot produce more than the limiting current because there are no reactants at the catalyst surface.

$$\Delta V_{conc} = \frac{RT}{nF}\ln\left(\frac{j_L}{j_L - j)}\right) \qquad (1.32)$$

The activation and concentration polarization can occur at both, anode and cathode electrodes. The total cell voltage is therefore

$$E_{cell} = E_r - (\Delta V_{act} + \Delta V_{conc})_{anode} - (\Delta V_{act} + \Delta V_{conc})_{cathode} - \Delta V_{omh} \qquad (1.33)$$

This potential is the actual experimental voltage measured when a single cell is tested. Figure 1.7 shows an example of how a fuel cell polarization curve is obtained by subtracting the activation polarization, concentration polarization and ohmic losses from the equilibrium potential [11,12].

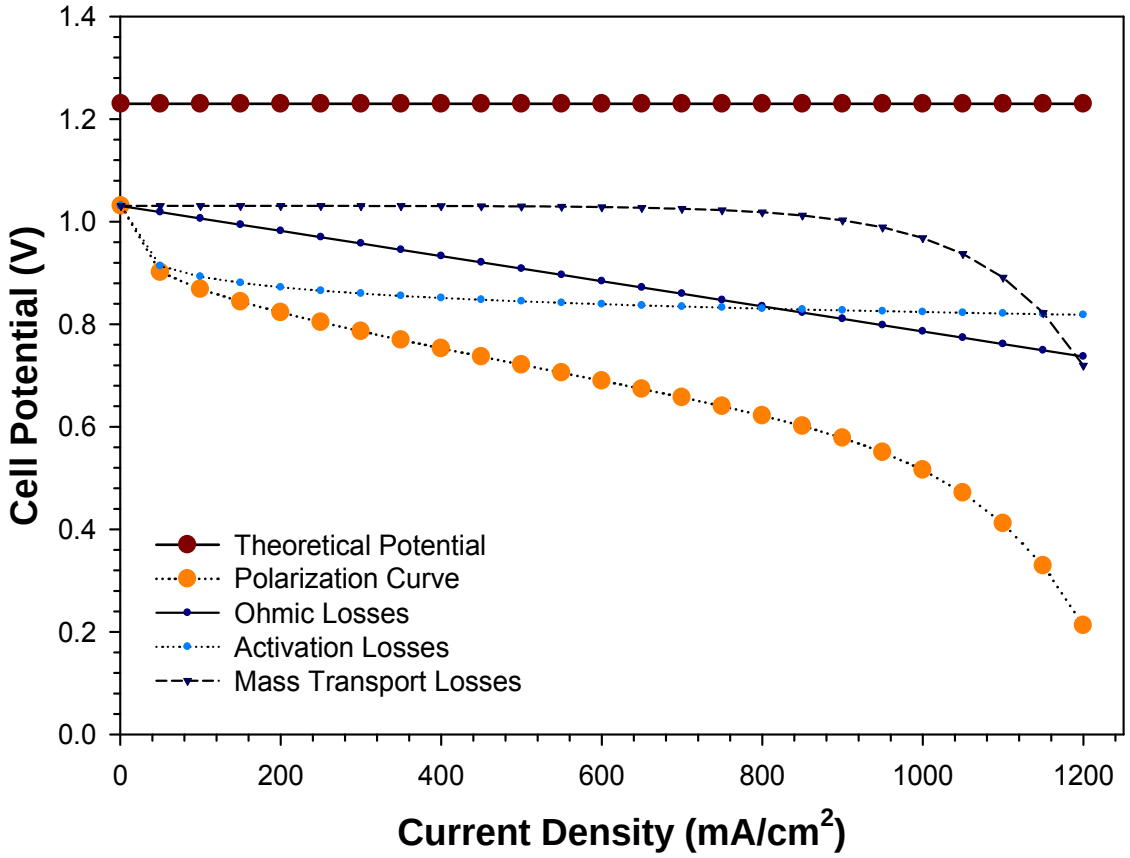

Figure 1.7. Fuel cell polarization curve [12].

2. NMR Diffusion Studies of Organic-Inorganic Composite Nafion Membranes

2.1. Introduction

The further development of polymer electrolyte membrane fuel cells (PEMFC) for mobile and stationary applications awaits the advent of a low-cost and high-temperature membrane, with suitable ionic conductivity and stability up to 150 °C. This would offer a potential solution to some of the drawbacks presently affecting PEMFC as well as direct methanol fuel cells (DMFCs) [1], including the effects of electrode poisoning by adsorbed CO molecules, limited methanol oxidation and oxygen reduction kinetics, and water and thermal management problems [2].

Composite perfluorosulfonic membranes based on Nafion containing hygroscopic ceramic oxides have been demonstrated to operate up to about 150 °C both in direct methanol [3-5] and hydrogen–air [2,6] polymer electrolyte fuel cells with reduced preheating temperature for the reactants (85 °C). By contrast, Nafion membranes without ceramic fillers may operate only up to 130 °C under elevated pressures (4 atm absolute pressure) and with higher reactants preheating temperature (120-140 °C) [4]. Additionally, the inclusion of inorganic fillers improves the mechanical properties and the membrane water management. It also inhibits the direct permeation of reaction gases by increasing the transport

This chapter is based on the paper: NMR investigations of water and methanol mobility in nanocomposite fuel cell membranes by I. Nicotera, A. Khalfan, G. Goenaga, T. Zhang, A. Bocarsly, S. Greenbaum. Ionics, 2008, **14**, 243.

pathway tortuousness [7]. The hydration properties of membranes are key characteristics that can influence the fuel cell performance. The composite membranes may also improve the water retention properties of these membranes under low humidity conditions. The conductivity of perfluorinated sulfonic acid membranes vary over many orders of magnitude depending upon the water activity and temperature. The PEMFC architecture, as well as materials and components, has some common features for both hydrogen and methanol operation. Therefore, it could be attractive to develop a unique membrane product for a flexible use in terms of fuels (hydrogen, methanol, reformate gas), operating temperature and application [8, 9]. In the present investigation, various composite membranes based on a Nafion matrix containing inorganic particles fillers (SiO_2, TiO_2, or $Zr(HPO_4)_2$) have been studied with particular emphasis on water and methanol transport properties. In fact, membrane conductivity and methanol cross-over are the most relevant issues to be addressed for high-temperature H_2 and direct methanol fuel cells, and these two properties are related to the mobility of water and methanol in the membrane [10]. Self-diffusion coefficients of water and methanol were measured using nuclear magnetic resonance (NMR) pulse gradient spin-echo (SE) [11].

Greater understanding of the mechanism of ion and molecular transport in polymers can be strongly assisted by employing pressure as the thermodynamic variable [12-14]. Variable pressure measurements can probe molecular motion and ionic diffusion processes associated with volume fluctuations.

2.2. Membranes preparation

The preparation procedure of filler-free Nafion membrane and organic–inorganic composite membranes of Nafion–SiO_2, Nafion–TiO_2, and Nafion–$Zr(HPO_4)_2$ ex-situ is reported in [15]. In addition, Nafion–$Zr(HPO_4)_2$ in-situ membrane was prepared by a different synthesis procedure involving the reaction of a solution of Zr^{4+} ions (from $ZrOCl_2$) with phosphoric acid (H_3PO_4) leading to the precipitation of the insoluble zirconium phosphate as described by Yang et al [16]. The $Zr(HPO_4)_2$ content for this membrane was 20 wt.% with respect to Nafion.

For NMR measurements, all the membranes were first dried over phosphorus pentoxide (P_2O_5) for several days, then were immersed in distilled water and in 2M methanol solution at room temperature for at least 2 days in order to obtain water-saturated and methanol saturated membranes. It is often possible in methanol–water mixtures to resolve spectroscopically the methyl and hydroxyl protons in an NMR experiment which, in principle, should permit the measurement of both water and methanol diffusion. However, in this case, the composite membranes presented a broad ^1H spectra with significant overlap of the CH_3 and OH peaks. Therefore, the methanol diffusion measurements were done on membranes equilibrated in a solution of natural abundance methanol in 99.9% D_2O (heavy water). The amount of water or methanol solution inside each membrane was determined by using a microbalance and recorded as:

$$Water\ uptake = \frac{Mass\ wet - Mass\ dry}{Mass\ dry} \times 100\% \qquad (2.1)$$

The membranes saturated with solvent (water or methanol solution) were removed from the liquid, quickly blotted dry with a paper tissue (to eliminate most of the free surface liquid), and loaded in sample holders (5-mm NMR Pyrex tubes) or polyethylene bags, which were then hermetically sealed.

2.3. NMR experiments

Temperature and pressure are the thermodynamic variables which determine the state of a solid. In some cases the pressure is a complementary variable to temperature, in other cases is the essential variable.

When temperature is varied at constant pressure, it affects molecular motions, changing the kinetic energy of the molecule and, changing the average volume available for the motion on the molecule. The use of pressure allows changing, in a controlled way, the intermolecular interactions without the major perturbation produced by changes in temperatures and/or chemical composition [16].

2.3.1. Variable temperature

Self-diffusion coefficients of water and methanol (DW and DM) were performed on a Chemagnetics CMX-300 spectrometer with ^{1}H operating frequency of

300.02 MHz, by using the pulsed field gradient spin-echo (PFGSE) method [11] with a gradient pulse length δ ranging from 0.8 to 1.2 ms, a delay time for diffusion of Δ of 10–12 ms, and varying the gradient amplitude from 10 to 300 G/cm. The measurements were done as a function of temperatures in the range of 25 to 140 ^{o}C.

2.3.2. High pressure

The pressure affects chemical equilibrium and reaction rates. The activation volume associated with ionic and molecular motion is a measure of the volume change of the materials as the ions or molecules pass from an equilibrium position to a saddle point [17]. It is defined as:

$$\Delta V = -\left[\frac{RT\partial \ln k}{\partial P}\right]_T \qquad (2.2)$$

where k is the reaction rate.

Studies in some liquids indicate that pressure effects can help to determine the mechanism of a specific dynamic process, while the temperature changes the frequency of the motions without affecting the mechanism. At high pressure, even at -15^{o}C water is still a liquid, which gives a powerful tool to study behavior of liquids as such low temperature, for example, protein denaturation.

The self diffusion coefficients obtained using NMR techniques are of great importance in the characterization of ionic conduction and molecular motion in polymer electrolytes. Molecular motion and ionic diffusion are associated with volume fluctuations that can be measured employing pressure as the thermodynamic variable. The activation volume associated to the diffusion coefficient can be written as:

$$\Delta V = -kT\left[\frac{\partial \ln D}{\partial P}\right]_T \qquad (2.3)$$

The naturally existing static field gradient of a conventional 7.3 T superconducting magnet was used to measure the water self-diffusion coefficients in membranes as function of an applied hydrostatic pressure. The central field and gradient strength were varied continuously, within the limits of the magnet, by moving the high-pressure NMR probe head within the bore of the magnet. The position of the radiofrequency coil (which contains the sample) determines both the resonant frequency and the magnetic field gradient.

A home-built, computer-controlled, motorized stage capable of moving the probe in precise steps of 0.25 mm was used to center the coil at a field gradient strength (G=dBz/dz) of 0.256 T/cm. This value was determined experimentally using the standard self-diffusion coefficient of water (2.299×10^{-5} cm^2 s^{-1} at 25 °C) and corresponds to the resonance frequency for protons of 72 MHz. Accurate variation of the pressure from 0 up to 2 kbar (in 0.25 kbar increments) was carried out using an Enerpac 11–400 hydraulic system fitted to a sealed Cu–Be

alloy high pressure chamber (bomb) inside of which resides the NMR radiofrequency coil and sample. A phase cycled spin-echo pulse sequence (π/2–τ–π–τ, acquire) was used to detect the proton echo signal from the sample. Pulse widths (π/2) were typically of 2.5 μs duration. This value was chosen on the basis of the maximum signal amplitude obtainable for a given pulse separation. Only two samples were tested by this technique: filler-free Nafion and Nafion–$Zr(HPO_4)_2$-ex situ with different initial water uptakes. The membranes were hermetically sealed in polyethylene bags to isolate them from the pressure transmitting fluid (hydrogen-free Fluorinert electronic fluid FC-77, manufactured by 3M Company). A diagram of the system in shown in figure 2.1.

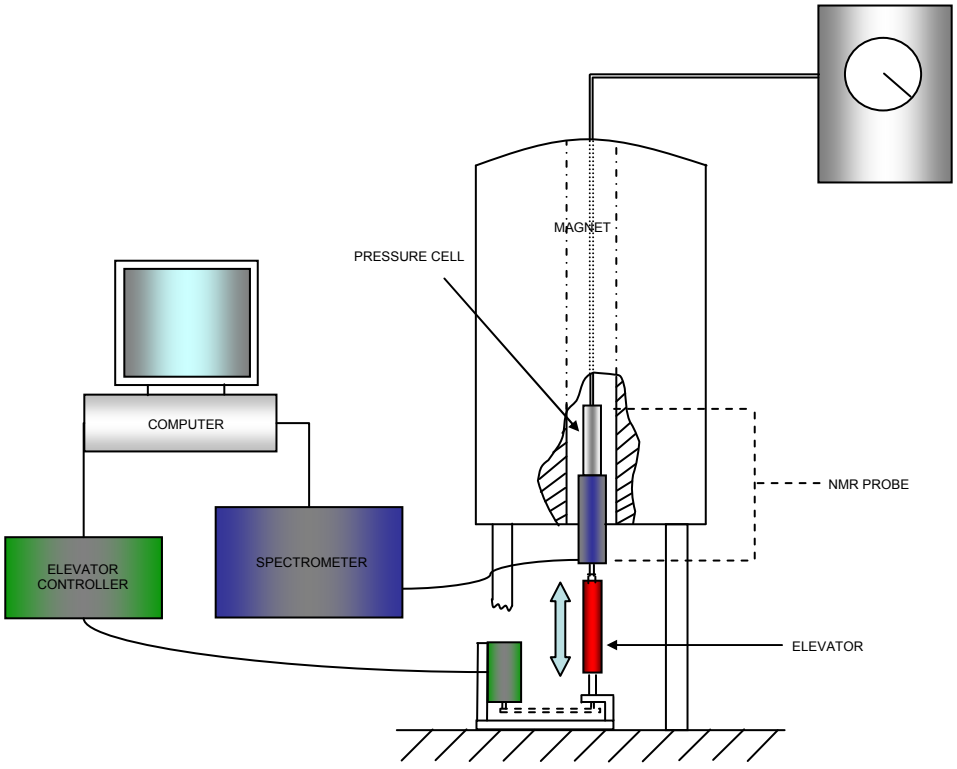

Figure 2.1. High pressure NMR set up.

2.4. Results and discussion

2.4.1. Water and methanol diffusion by PFGSE–NMR

Composite membranes based on Nafion and the filler-free Nafion membrane were swelled by immersion in both, 2M methanol solution and in pure water. The correspondent saturation uptake values are shown in Table 2.1.

Membranes	2 M MeOH uptake (%)	Water uptake (%)
Nafion filler-free	35	37
Nafion-SiO_2	56	46
Nafion-TiO_2	46	50
Nafion-$Zr(HPO_4)_2$ ex situ	45	60
Nafion-$Zr(HPO_4)_2$ in situ	26	34

Table 2.1. Methanol and water uptakes of the membranes at room temperature.

The uptakes of filler-free Nafion in 2M methanol and in water are very close, i.e., it can adsorb no more than ~35 wt.% of solvent to reach the highest swelling state. The effect of adding filler particles is generally to increase the water uptake.

However, Nafion–$Zr(HPO_4)_2$ in-situ composite departs from this behavior. It is important to highlight some differences between the two solvents. For example, Nafion–$Zr(HPO_4)_2$ ex-situ sample swelled in pure water has a greater uptake (60

wt.%) than the other composites; but when the solvent is 2M methanol solution, the uptake is reduced to 45 wt.%. The opposite behavior is observed in the silica composite that shows the highest methanol solution uptake (56 wt.%) but a comparatively low water uptake (46 wt.%). Finally, the titania composite does not show particular preference for one of the two solvents.

Self-diffusion coefficients of water and methanol were measured by PFG-NMR technique on the completely swelled membranes in the temperature range from 25 to 140 °C, the results are shown in figure 2.2. The first evident outcome is that the water diffusion is higher than the methanol diffusion in all the samples for the investigated temperature range. This difference is particularly accentuated in both Nafion–$Zr(HPO_4)_2$ composites, where the difference is about a factor of 2. Table 2.2 lists the diffusion coefficient values for both, water and methanol, at 25 and 100 °C.

In general, the composites membranes present higher water diffusion than the filler-free Nafion at both, low and high temperatures, with particularly high values for the Nafion–$Zr(HPO_4)_2$ ex-situ composite. The only exception is presented by Nafion–$Zr(HPO_4)_2$ in-situ composite that shows the lowest diffusion coefficients.

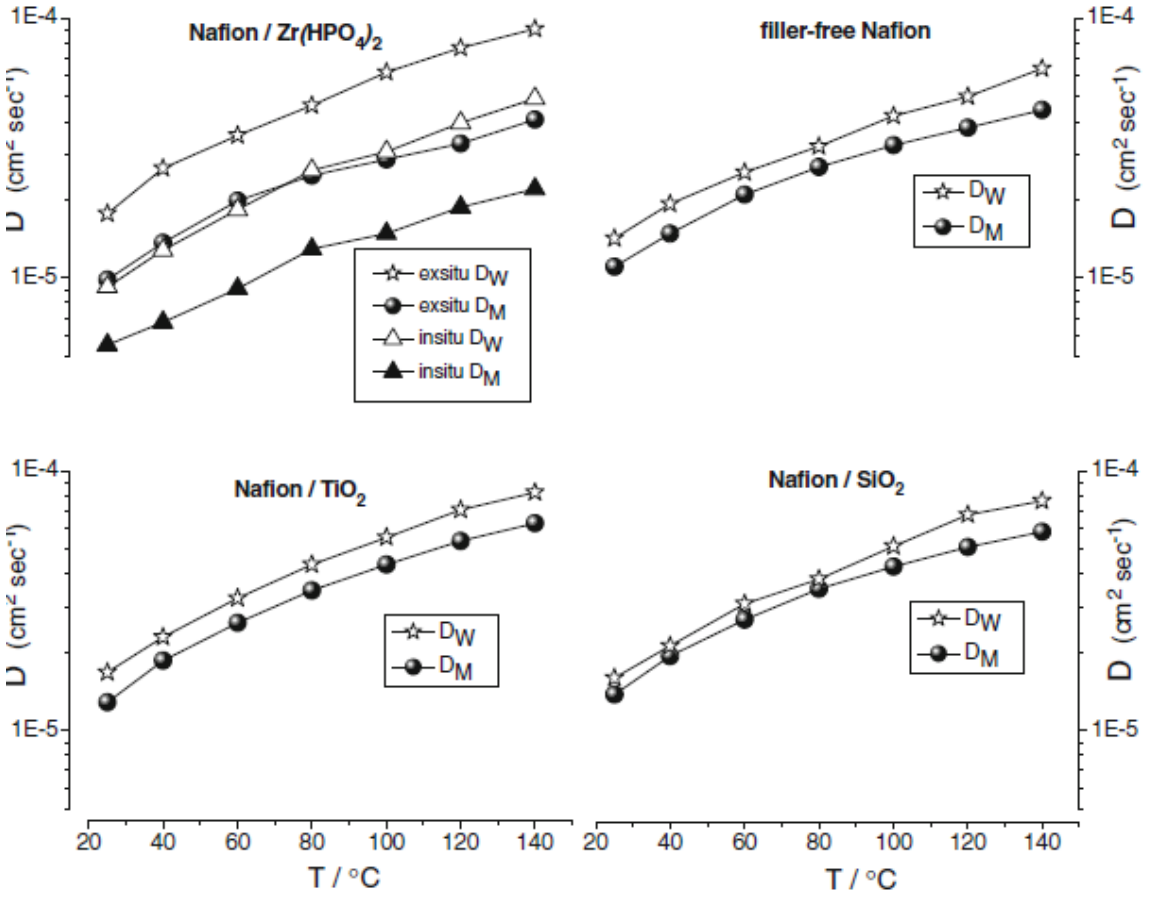

Figure 2.2. Self diffusion coefficients of Methanol (D_M) and water (D_W). Completely swelled membranes with temperature between 25 and 140 °C.

Membranes	D_M (x 10^{-5} cm^2 sec^{-1})		D_W (x 10^{-5} cm^2 sec^{-1})	
	25 °C	100 °C	25 °C	100 °C
Nafion filler-free	1.10	3.24	1.42	4.20
Nafion-SiO_2	1.37	4.28	1.59	5.12
Nafion-TiO_2	1.28	4.36	1.67	5.54
Nafion-$Zr(HPO_4)_2$ ex situ	0.98	2.83	1.76	6.20
Nafion-$Zr(HPO_4)_2$ in situ	0.55	1.48	0.92	3.06

Table 2.2. Self diffusion coefficients of Methanol (D_M) and water (D_W), in completely swelled membranes.

Methanol diffusion shows a slightly different behavior: in the silica and titania composites, methanol molecules are more mobile than in the filler-free Nafion while both $Zr(HPO_4)_2$ in-situ and $Zr(HPO_4)_2$ ex-situ composites exhibit the lowest methanol diffusion coefficients. A previous study established the strong relationship between water uptakes and diffusion coefficients, the systems which absorb more water exhibit the higher diffusivity [15]. In particular, $Zr(HPO_4)_2$ ex-situ with 60 wt.% of water uptake shows the highest diffusion coefficients followed by TiO_2, with 50 wt.%, SiO_2 with 46 wt.%, filler-free Nafion with 37 wt.%, and finally $Zr(HPO_4)_2$ in-situ that absorbs only 34 wt.% water. However, this correlation between diffusivity and solvent absorbed does not hold for methanol. For instance, the uptake of the filler-free Nafion is 35 wt.% against the 45 wt.% of the $Zr(HPO_4)_2$ ex-situ composite, but the corresponding methanol diffusion coefficients are almost identical or even slightly greater in filler-free Nafion. The Nafion–SiO_2 and the Nafion–TiO_2 composites reveal a comparable methanol diffusivity, but the silica composite absorbs 56 wt.% and the titania composite only 46 wt.%.

However, the elevated amount of solution absorbed by the silica membrane does not contribute to increase the diffusion, as was expected. It could be claimed that in the presence of a solution of methanol in water, a competition between methanol molecules and water molecules for the adsorption on the silica surface may arise.

Another study reports that methanol has higher affinity than water to silica, because it displaces water molecules from the silanol groups and thus breaks the H bond network within the hydration sheath around silica [18]. As a result, the chemical affinity favors methanol uptake with respect to the water, but the strong coordination of the methanol molecules on the silica surface restrains their mobility. This last effect could be responsible for the lower methanol diffusion when compared to water in all the membranes, including the filler-free Nafion. In fact, not only the interaction between the fillers surfaces and the oxidrilic groups of methanol molecules but also the stronger interactions of these with the sulfonic groups of the polymeric side chains of the Nafion can contribute to impede the molecules' transport.

2.4.2. Water diffusion by high-pressure NMR

Water diffusion measurements were collected as function of the pressure applied to the membrane in order to probe molecular motion process associated with volume fluctuations. In the high pressure experiment, the proton spin echo intensities M(τ) were measured as a function of the pulse separation τ. The self diffusion coefficients D were obtained from the data using the equation

$$M(\tau) = M_0 \exp\left[-\frac{2}{3}\left(\frac{3\tau}{T_2} + \gamma^2 g^2 D \tau^3 \right) \right] \qquad (2.4)$$

where M_0 is the maximum magnetization.

The proton spin spin relaxation times T_2 were measured independently, and the data was fit to a linearized version of equation (2.4) with slope $2/3(\gamma g)^2 D$ and intercept $2/T_2$. The self diffusion coefficients were obtained as a function of pressure. Figure 2.3 shows the self-diffusion coefficients collected on filler-free Nafion as function of pressure for three different water uptakes: 30%, 20%, and 10%. For comparison, we also analyzed Nafion–$Zr(HPO_4)_2$ ex-situ membrane at 30 and 20 wt.% of water uptake because it showed the best water diffusion behavior at ambient pressure.

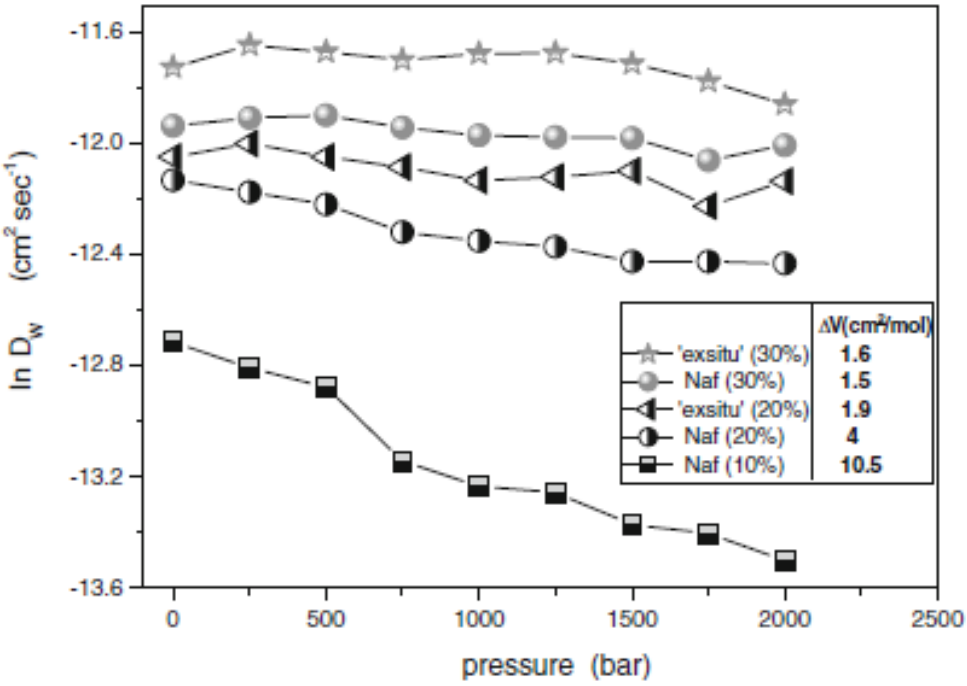

Figure 2.3. Water self-diffusion coefficients (D_W) measured by high pressure NMR. Partially swelled filler-free Nafion and Nafion/$Zr(HPO_4)_2$ ex-situ composite membranes.

The self-diffusion coefficient generally decreases with increasing pressure reflecting the greater restrictions for water molecular motions. In the plot are also listed the activation volume ΔV associated with the diffusing water molecules and calculated according to equation (2.3).

It was observed that the activation volume increases with decreasing water content. However, it is useful to comment further on the obtained values: at water content of 30 wt.%, both filler-free Nafion and $Zr(HPO_4)_2$ composite activation volumes are relatively small but comparable. In this region, however, it is likely that the diffusion is controlled by bulk water more than by the polymer. Instead, at water content of 20 wt.%, the difference between the activation volumes of two systems is considerable: 4 cm^3/mol for filler-free Nafion and 1.9 cm^3/mol for Nafion–$Zr(HPO_4)_2$ ex-situ composite. A relatively large ΔV of 10.5 cm^3/mol is observed for 10% water content in filler-free Nafion membrane. The observation that high activation volumes are often associated with solvent-free polymer electrolytes suggests that ion transport in these cases is controlled by polymeric segmental motion [12,19]. The highest activation volume we have seen here is lower than the values usually associated exclusively with segmental motion. It is surmised that significantly higher values of ΔV would be observed for nearly dry membranes (<10% water), but the proton NMR signal strength is insufficient to verify this. Nonetheless, in the single case where comparison between filler-free and composite Nafion with comparable water contents (20%) is possible, the factor of 2 difference in ΔV suggests a significant difference in water transport properties consistent with the modified pore or channel structure of the composite [15].

2.5. Conclusions

NMR diffusion measurements were done on Nafion composite membranes to understand better their water and methanol uptake and transport characteristics. With the exception of the $Zr(HPO_4)_2$ added in-situ to the membrane, all the other composites, made with $Zr(HPO_4)_2$ (ex-situ), TiO_2, and SiO_2, showed enhanced water retention and protons mobility compared to filler-free Nafion. However, for 2M methanol solution only SiO_2 and TiO_2 showed diffusion improvement with respect to the filler-free Nafion.

All results are consistent with modified pore structure attributable to the filler particles, including the observation of a reduced diffusion activation volume in the composite relative to filler-free Nafion.

3. Aligned Carbon Nanotubes based MEAs

3.1 Introduction

The anode and cathode electrodes in polymer electrolyte membrane fuel cells (PEMFC) consist of the mix of porous carbon supported catalyst and an ion conducting polymer (ionomer). The most common materials used are Pt/carbon black (CB), and Nafion® solution, mixed in the form of an ink. The membrane electrode assembly (MEA) is formed by depositing this ink on both sides of a Nafion polymer membrane [1]. Though convenient and economical, the ink method for electrodes preparation presents certain disadvantages to the FC performance. For instance, CB is amorphous carbon, formed by particles that are randomly distributed and interconnected inside the carbon structure. This particles interconnection allows electronic and thermal conduction in the electrode. But CB degrades easily in the corrosive environment such as that found in cathode of the fuel cell, the carbon particles shrink due to oxidation under the FC high operation potentials, causing the loss of contact between particles and as a consequence the loss of electronic and thermal conductivity. In addition, CB is hydrophilic and tends to retain water, causing flooding issues, which prevents the reactant gases from reaching the catalytic sites. On the other hand, due to the carbon structure the Pt catalyst exposure is not completely optimized and it is estimated that only 40% of the Pt deposited on the carbon

This chapter is based on the papers: “Polymer electrolyte fuel cell with vertically aligned carbon nanotubes as the electrocatalyst support” by J. Yang, G. Goenaga, A. Call, D.J. Liu. Electrochemical and Solid State letter 2010, 13, B55. “Performance improvement in PEMFC using aligned carbon nanotubes as electrode catalyst support” D-J Liu, J. Yang, N. Kariuki, G. Goenaga, A. Call, and D. Myers. ECS Transactions, 16 (2) 1123-1129 (2008)

support is utilized during the oxidation and reduction reactions in the anode and cathode, respectively. Furthermore, the random distribution of the carbon particles in the CB matrix, generates a tortuous path for the flow of the reactant gases to the catalytic sites, and contributes to the flooding problems. Pt is a precious metal that has limited resources and is very costly, representing about 40% of the FC cost. The amount of Pt used in the cathode electrode is about 4 to 5 times higher than in the anode due to the slower oxygen reduction reaction [2]. The ionomer is used to enhance to the proton conduction in both electrodes and to keep together the catalyst particles, acting as binder. The amount of ionomer used to prepare the ink has an impact on the MEA performance, too little can lead to poor proton conduction and poor catalyst adhesion to the membrane, while too much ionomer can block the gas flow to the active sites, and limit the oxidation and reduction reactions. Figure 3.1. shows a schematic representation of this approach.

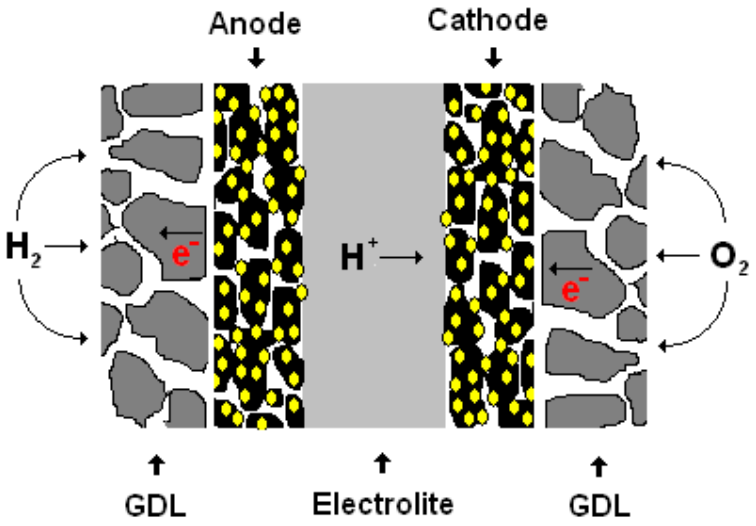

Figure 3.1. Ink-based MEA using CB as the Pt support.

It is then necessary to improve the electronic and thermal conductivity, reduce the amount of Pt catalyst by optimizing the distribution of Pt nanoparticles on the carbon support, while finding the optimum ionomer amount for the proper functioning of the FC.

As an alternative, carbon nanotubes could surpass CB as better Pt support, because they are better electron conductors, possess higher geometric surface area and their graphitic structure makes them more resistant to the acidic environment and the oxidative conditions on the PEMFC cathode. The electronic and thermal conduction is accomplished along the graphitic walls of the nanotubes, avoiding the loss of contact. In addition, they are hydrophobic, a characteristic that makes them ideal to solve flooding issues, especially during water formation in the cathode electrode. In particular, if growing in vertically aligned structures of parallel tubes, they can provide direct paths for the reactant gases to reach the catalytic sites, what can potentially improve the mass transfer in the FC. Moreover, their high geometric area allows a uniform distribution of the Pt nanoparticles on the nanotubes walls, placing the catalytic sites directly in the path of the reactant gases, which avoids the tortuousity of the CB matrix and can potentially improve the mass transfer with lower Pt usage. The aligned carbon nanotubes (ACNTs) can also connect directly the MEA to the current collector plates, eliminating the necessity of using a GDL. The proton transfer can be accomplished by coating the ACNTs with a very thin, gas-permeable ion-conducting layer prepared with a diluted Nafion® ionomer solution [3,4].

The above mentioned advantages make ACNTs an ideal Pt support, with promising improvement of the cell performance while decreasing the amount of Pt catalyst used, particularly in the cathode electrode. For this investigation, MEAs were prepared using CB as the Pt support in the anode and ACNTs in the cathode, as is represented in Figure 2.

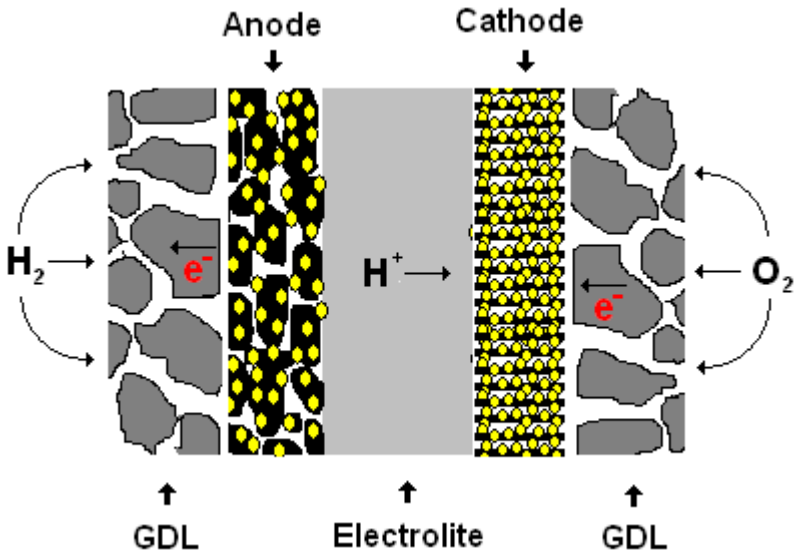

Figure 3.2. MEA using ACNTs as the Pt support for the cathode electrode.

3.2 Electrodes Preparation

The anode and the cathode are prepared using different techniques, which are described below.

3.2.1 Anode preparation

The anode is ink-based. The ink is prepared using BASF C1 20-20% Pt on Vulcan XC-72 as the platinum-carbon precursor. This precursor is mixed with 5 wt% Nafion® solution, Tetrabutylammonia hydroxide (TBAOH) and glycerol. The resulting mix is stirred thoroughly on a magnetic plate until it reaches the desired consistency. The total Nafion to Pt/C ratio is 2 to 5 by mass. 5 cm^2 substrates (decals) are prepared using a fiber glass sheet coated with polytetrafluoroethylene (PTFE). In order to facilitate the transfer of the electrode, an additional fine layer of PTFE in aerosol is sprayed onto the decals.

A camel hair brush is used to paint the ink on the decals, following the method described by Wilson and Gottesfeld [1]. Several layers of the ink are painted until the decals reach the target weight. After each added layer, the decals are dried in an oven at 140 ^oC for 1 hour, and then are weighed. In this case, the target weight was 0.2 mg Pt/cm^2, or the equivalent of 7 mg of gained weight on a 5 cm^2 decal. When a weight slightly higher than 7 mg is reached, the samples are dried overnight at 140 ^oC, to evaporate the solvents completely, and weighed again. Table 3.1 shows an example of a batch of ink decals prepared using this technique. Columns L1-L5 show the weight gained after each layer of ink is painted on the decals. The last column shows the final weight after the samples are dried overnight.

Sample	W_o	L1	L2	L3	L4	L5	Overnight	W_f
117A	0.2460	0.2470	0.2485	0.2499	0.2517	0.2537	0.2529	
Change		0.0010	0.0025	0.0039	0.0057	0.0077	0.0069	**0.0069**
117B	0.2462	0.2471	0.2485	0.2504	0.2522	0.2544	0.2534	
Change		0.0009	0.0023	0.0042	0.0060	0.0082	0.0072	**0.0072**
117C	0.2601	0.2611	0.2626	0.2641	0.2658	0.2680	0.2671	
Change		0.0010	0.0025	0.0040	0.0057	0.0079	0.0070	**0.0070**
117D	0.2561	0.2573	0.2586	0.2602	0.2617	0.2636	0.2628	
Change		0.0012	0.0025	0.0041	0.0056	0.0075	0.0067	**0.0067**
117E	0.2524	0.2539	0.2550	0.2567	0.2582	0.2601	0.2593	
Change		0.0015	0.0026	0.0043	0.0058	0.0077	0.0069	**0.0069**
117F	0.2511	0.2524	0.2537	0.2552	0.2574	0.2593	0.2587	
Change		0.0013	0.0026	0.0041	0.0063	0.0082	0.0076	**0.0076**

Table 3.1. Ink decals painting process. L1 to L5 refer to the weight after each layer, W_o and W_f refer to initial and final weight respectively. All the weights shown are in grams.

3.2.2 Cathode preparation

3.2.2.1 Aligned Carbon Nanotubes synthesis and characterization

The aligned carbon nanotubes are synthesized using chemical vapor deposition (CVD) with a xylene-ferrocene solution as the precursor. Xylene is the carbon source, while ferrocene provides the iron metal nanoparticles, which function as the seeds for the nanotubes growth. Three 5 cm^2 quartz substrates are placed inside an 1 inch diameter quartz reaction tube. Figure 3.3. shows a schematic representation of the reaction tube. The tube is placed in a two stage furnace and tightly sealed to air. The first stage of the furnace is at a temperature of 225 ^oC, which is enough to vaporize the solution. The second stage is held at 725 ^oC and is used to carbonize the vaporized solution, depositing the iron nanoparticles on the quartz substrates, and allowing the carbon nanotubes to grow around the

iron seeds. The solution with the chemicals is injected into the reaction tube, on the low temperature stage, using argon and hydrogen as the carrier gases, at flow rates of 100 and 50 mL/min respectively. The chemicals injection rate is 0.225 mL/min.

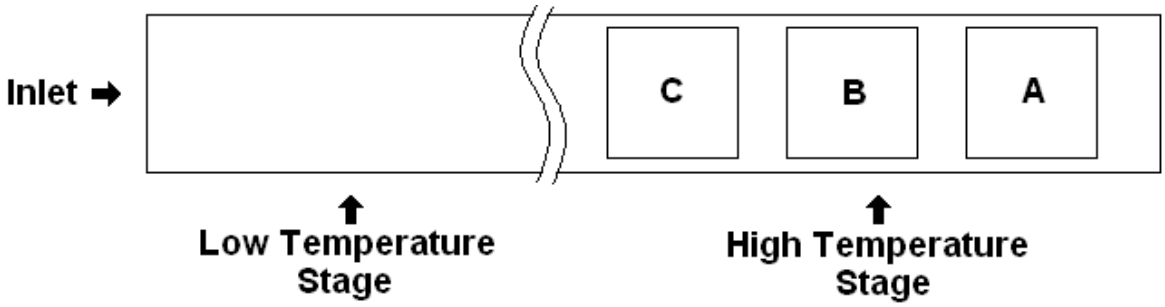

Figure 3.3. Diagram of the reaction tube and substrates position.

Before preparing ACNT-MEAs it is important to determine characteristics of the ACNTs, such as the loading, length, uniformity and their dependence on the growth time and substrate position inside the reaction tube.

The weight (loading) and length of the nanotubes depend on the growth time. Shorter the time, shorter the tubes, and lower the loading. The obtained nanotubes are multi walled and have typical lengths of 10-15 μm, 15-20 μm and 20-25 μm for 5, 8 and 15 minutes growing time, respectively, as determined from SEM images of the samples. The diameter ranges from 10 to 100 nm, and the density is between 10^8 to 10^9 tubes per cm^2, proportional to the chemicals injection rate. The loading of the nanotubes also depends directly on the growing

time, at longer time more carbon is deposited on the substrates, which logically can be deduced from the length-time dependence. The loading also depends on the position of the substrates inside the reaction tube. Figures 3.4. shows SEM images of the as-synthesized ACNT.

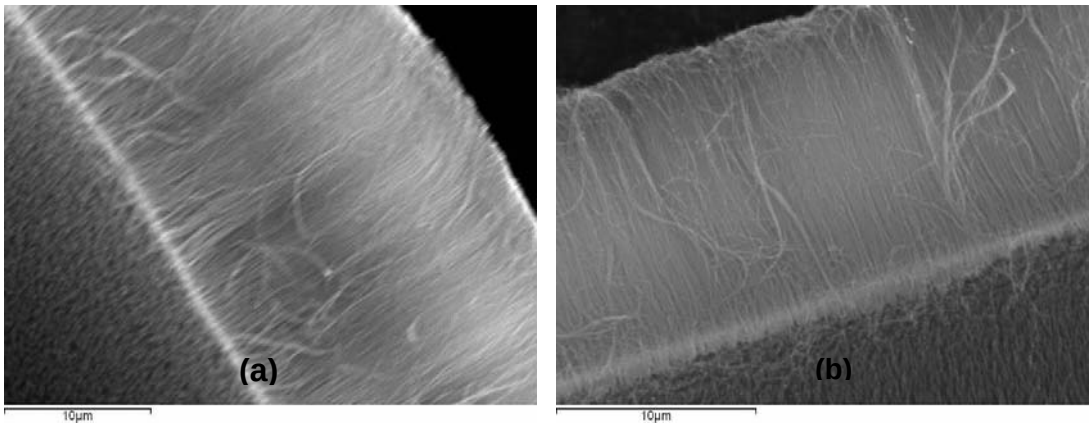

Figure 3.4. SEM images of xylene-ferrocene ACNT bundles. (a) for 8 minutes and (b) for 5 minutes growing time.

Normally, the sample closer to the chemicals and gases inlet (sample C) gets the lower loading, and the one in the middle (sample B) the highest (see Figure 3.3). This pattern can be attributed to the fact that the gas flow inside the reaction tube is turbulent when it hits the first substrate inside the reaction tube, stabilizing and becoming laminar when it reaches the second substrate and becoming less laminar on top the third substrate, due to the furnace configuration. Figure 3.5. shows a bar graph of the weight dependence on the growing time, for typical batches of ACNTs.

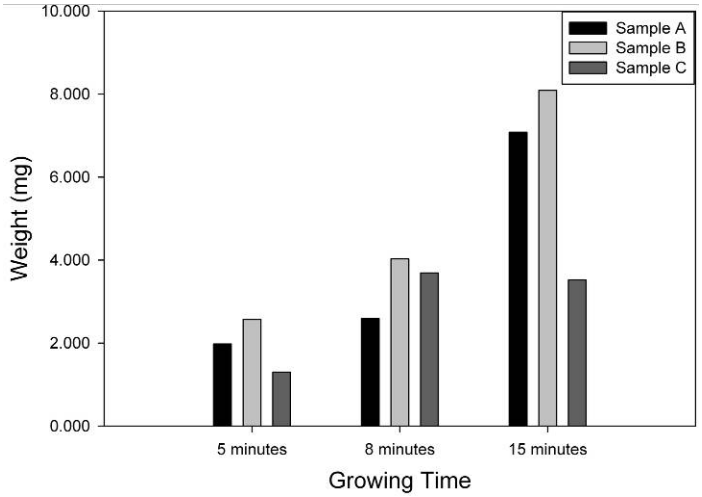

Figure 3.5. Loading vs. Time dependence. Longer growing time produces longer and heavier nanotubes, the loading also depends on the position of the substrate inside the tube.

The uniformity of the ACNTs also depends on the substrate position inside the tubes, with samples in position B being the most uniform, followed by samples in position A. The uniformity of the samples was determined using four point conductivity measurements, measuring the resistance at three different points on each sample. The resistance is inversely related to the length, longer tubes have lower resistance, which can be used to map the uniformity of the nanotubes. Figure 3.6 shows resistance measurements for samples B at different growing time, position 1, 2 and 3 refers to where the resistance was measured on top of the sample. Samples from B were generally used to fabricate the MEAs for this investigation.

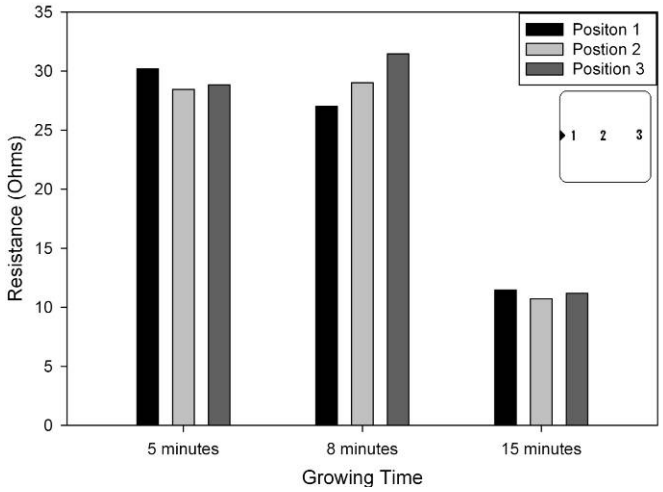

Figure 3.6. Conductivity measurements to determine ACNTs uniformity.

3.2.2.2 Catalyst deposition on the ACNTs

The Pt catalyst deposition on the ACNTs posed one of the major challenges in this project. For this application it is required to have a uniform distribution of Pt nanoparticles along the nanotubes walls, without destroying the alignment of the nanotubes layer on top of the quartz substrate. Among various techniques available, wet chemistry seemed to offer the best alternative because its simplicity and low cost. In this technique, an aqueous Pt containing solution is applied to the nanotubes. When the solution penetrates between individual tubes, soaking them completely, Pt nanoparticles bond to the nanotubes walls due to strong Van der Waals interactions. However, the high hydrophobicity of the ACNTs prevents them from getting wet by water based solutions, Figure 3.7(a). An initial attempt to overcome the hydrophobicity was to oxidize the

nanotubes with water vapor at high temperature and make them more hydrophilic. Although, after the vapor treatment, the nanotubes wet better, the ACNTs layer was being destroyed and removed from the quartz substrates. A different approach was to find organic chemicals that can wet the hydrophobic surface yet mix well with water. After many trials with different Pt precursors, including Pt sulfite, Pt Acetonate, and Chloroplatinic Acid (CPA) we found that a solution of CPA, water and tetrahydrofouran (THF) wets the nanotubes well, keeping intact the alignment, Figure 3.7(b).

(a) (b)

Figure 3.7. Wet chemistry technique for catalyst deposition on ACNTs. (a) Water drops on the ACNTs, high hydrophobicity, (b) modified wet chemistry method.

The Pt content in the catalyzing solution may be varied between 2.5 and 5 wt% Pt. In order to control the Pt loading, fine layers of the solution are sprayed on the ACTNs using an air brush, and the sample is weighed until it reaches the desired amount of Pt. Pt is then reduced to Pt metal by heat treating the

samples for 1 hour under hydrogen at 300 ^{o}C. Figure 3.8 shows examples of TEM images of Pt catalyzed carbon nanotubes.

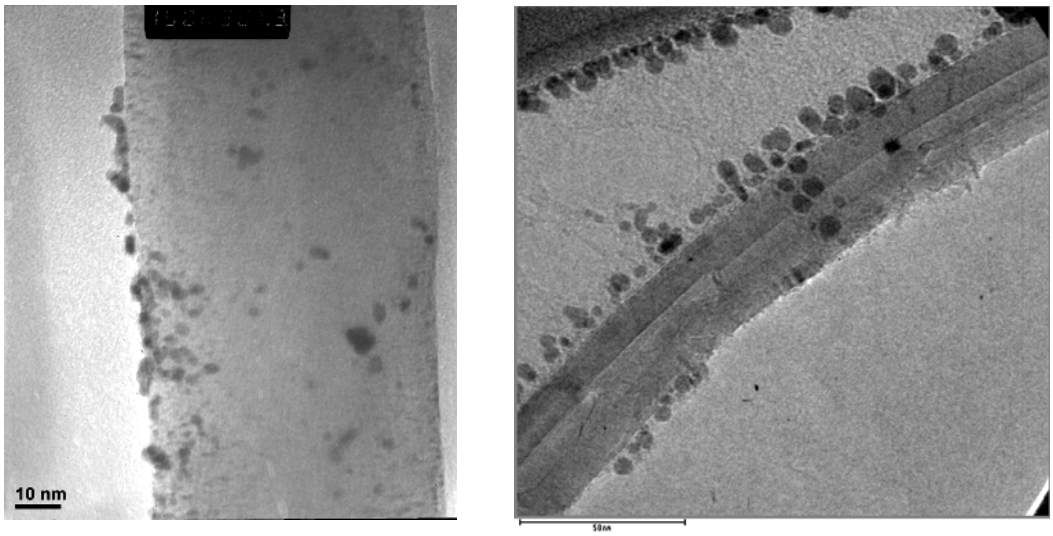

Figure 3.8. TEM images of Pt metal crystallites dispersed along the ACNTs.

The airbrush spray of the aqueous Pt precursor tends to produce larger metal crystallites than the conventional ink preparation method, although the particle size depends strongly on the precursor concentration and the number of applications. The particles deposited have typical sizes between 3.5 and 10 nm. Electron dispersive spectroscopy (EDS) study shows that Pt is evenly distributed through the depth of the highly hydrophobic ACNTs layer.

Following the Pt reduction, 1 wt% Nafion solution is sprayed onto the nanotubes to improve the proton conduction, and to facilitate the transfer of the ACNTs electrode layer during the MEA fabrication.

3.3 ACNT-MEA preparation

In order to assemble the MEA, a 10 cm^2 piece of Nafion 112 membrane is first converted to the sodium form by boiling it in 0.1 M NaOH for 1 hour. This makes Nafion more resistant to high temperatures and facilitates the electrode adhesion to it. Both, anode and cathode, electrodes are transferred to the Nafion membrane using the hot press method. This method consists in making a "sandwich" with the ink-based anode, the membrane and the ACNT-based cathode. The MEA components are protected placing them in the middle of rubber sheets and aluminum plates. The temperature of the press is set at 200 ^oC and a pressure of 600 psi is applied. After five minutes under pressure the "sandwich" is removed from the press and cooled down to room temperature. The anode and cathode substrates are removed carefully, leaving as a result the electrodes firmly adhered to the membrane. The thus formed MEA is converted back to the proton form, boiling it in 0.5 M H_2SO_4 and DI water.

Figure 3.9 shows a SEM image of an ACNT-MEA cross-section. The top layer is the cathode, formed by the catalyzed ACNTs, showing a uniform thickness and alignment. The middle layer the Nafion 112 membrane and, the bottom one is the ink based anode. As can be seen, the nanotubes alignment is intact after the high pressure hot transfer, confirming the high mechanical strength of the ACNT layer as previously demonstrated [5]. The ACNTs bind well with the membrane electrolyte and cannot be easily removed by bending or scratching of the film.

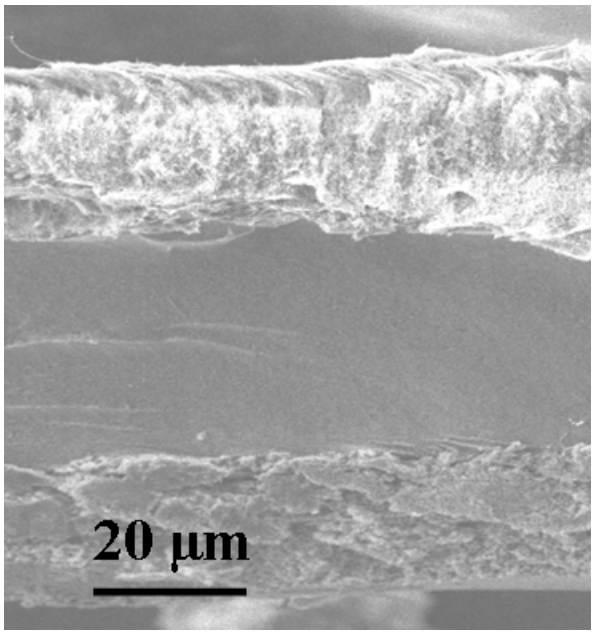

Figure 3.9. ACNT-MEA cross section.

3.4. ACNT-MEA PEMFC single cell test

The ACNT-MEA has a 5 cm^2 active area and for its testing is mounted in a single cell, with graphite bipolar plates and a single-serpentine flow field. Commercially available carbon cloth treated with Teflon is used as the GDL for anode and cathode, and inserted between the MEA and the bipolar plates. The single cell is attached to an Electrochem Inc. test stand to record the I-V polarization curves, which gives a measurement of the MEA's performance. The cell is initially conditioned for a few hours until it reaches the desired temperature and humidity conditions, using argon gas in the anode and oxygen gas in the cathode, at a constant voltage of 0.4 V, according to the US Fuel Cell Council

test protocol [6]. After a constant current is reached, the polarization curves are measured by potentiostatically cycling the voltage between 0.2 and 1 V. All tests are conducted at a cell temperature of 75 ^{o}C with hydrogen gas in the anode and air or oxygen gas in the cathode, both gases at relative humidity of 100%. The gas flow rates are 100 sscm at 1.2 bar and 300 sccm at 1.5 bar for the anode and cathode, respectively.

Figure 3.10 shows a comparison of the I-V polarization curves of an ACNT-MEA and a commercially available ink-based MEA that was used as a benchmark. The ACNT-MEA used for this test has an ACNT cathode layer with an approximate thickness of 20 μm and a Pt loading of 0.45 mg Pt/cm^2, and an ink-based anode with 0.2 mg Pt/cm^2. The commercial MEA uses a Nafion 112 membrane electrolyte and has Pt loadings of 0.5 mg Pt/cm^2 for both, anode and cathode.

In the kinetically limited region, where the current is close to zero, little difference is observed between ACNT-MEA and the commercial product because they both are Pt based electrocatalysts. In the high current region, the I-V curve extends further for ACNT-MEA, suggesting a significant reduction of the overpotential from the mass-transport limit. Correspondingly, the power density improves in the high current region. This observation demonstrates experimentally that improved interaction between the reactant gases and the catalyst sites can indeed be achieved by the ACNT electrode structure. The performance

improvement in the high current region can be attributed to lower mass transfer resistance to air on the ACNTs surface, what facilitates its access to the catalytic sites. Also, a more effective removal of the excess water formed during the oxygen reduction can be accomplished on the hydrophobic nanotubes surface.

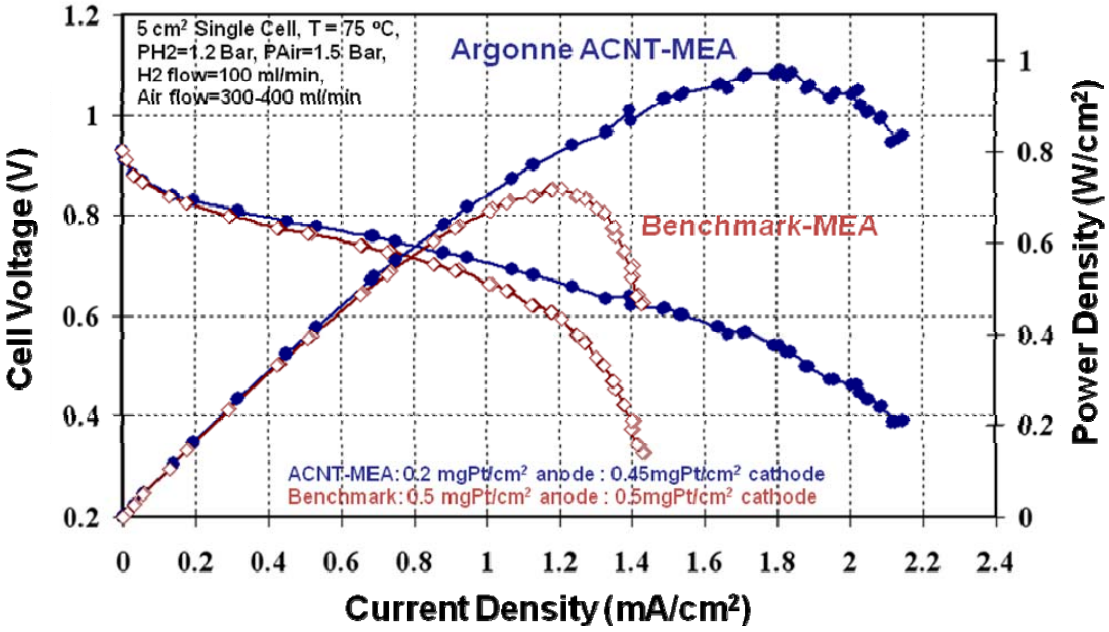

Figure 3.10. Comparison between ACNT-MEA and benchmark ink-based MEA performance.

In addition to the polarization curves, diagnostic tests including durability, impedance spectroscopy and cyclic voltammetry were carried out to determine the cell ohmic resistance and MEA electrocatalytic surface area.

In order to determine the stability of the ACNT-MEA and how it compares to the benchmark MEA, accelerating aging tests were carried out, as well as measurements of the electrochemical surface area (ECSA). After the initial I-V polarization curves are taken for both MEAs, the cells are potentiostatically cycled between 0.5 and 1.4 V using hydrogen gas in the anode and argon gas in the cathode. In this case the anode is used as the reference electrode/counter electrode, and the cathode as the working electrode. Cycling at these high potentials simulates operation of the cell for long periods of time. After 300 cycles, oxygen gas is then flown in the cathode and new I-V polarization curves are taken. Figures 3.11 and 3.12 show the results of these tests for both MEAs. As can be observed from these graphs, the ACNT-MEA presents higher stability than the ink based MEA over the 300 cycles.

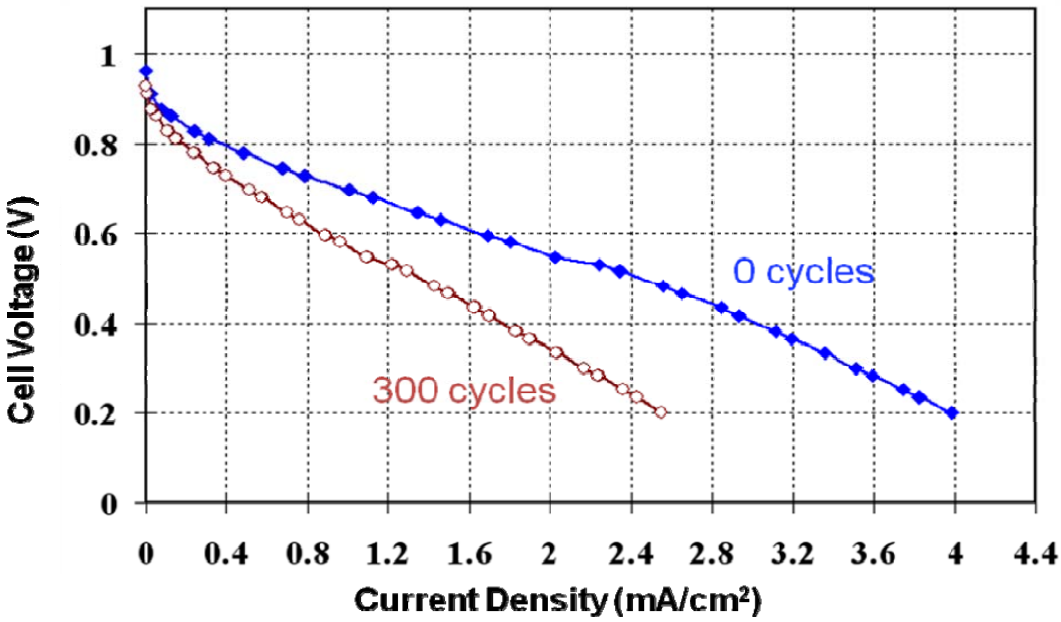

Figure 3.11. I-V polarization curves showing performance of ink-based benchmark MEA before and after accelerated aging test.

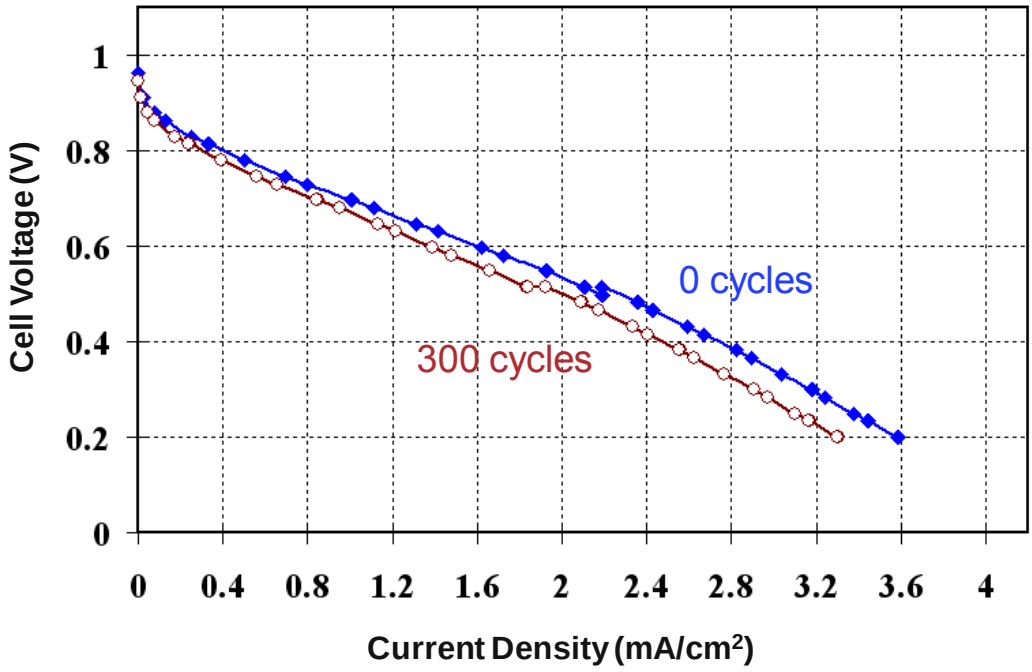

Figure 3.12. I-V polarization curves showing ACNT-based MEA performance before and after accelerated aging test.

From figure 3.11, we can observe that at 0.6 V the current output of the ink-based MEA after 300 cycles decreases to about 50% of its initial value. In contrast, figure 3.12 shows that at the same voltage and under the same aging conditions, the ACNT-MEA current output decreases only by 15% of its initial value.

During cycling the electrochemical surface area (ECSA) was also measured. The ECSA is a measure of the number of catalytic sites that participate in the catalytic reaction in the electrodes. The ECSA of the platinum nanoparticles in the ACNT-MEA cathode electrocatalyst was determined by calculating the charge necessary for adsorption and desorption of a monolayer of hydrogen

atoms on the platinum surface. The reaction of protons to produce a monolayer of adsorbed hydrogen atoms and the corresponding desorption of these hydrogen atoms occurs in the 0.07 to 0.45 V potential region. The voltage on the cathode side of each cell was scanned versus the anode side between 0.07 V and 0.5 V at 10 mV/s until a reproducible voltammogram was obtained. The ECSA was determined by integrating the double layer-corrected charge of the anodic-going scan in the 0.07 to 0.4 V region. The ECSA was calculated by assuming a charge of 210 mC/cm² in the hydrogen desorption region [7].

Initially, the value of ECSA for ACNT-MEA is about 60% of the value for the ink-based MEA. Figure 3.13 shows the change in percentage of ECSA for both MEAs. .

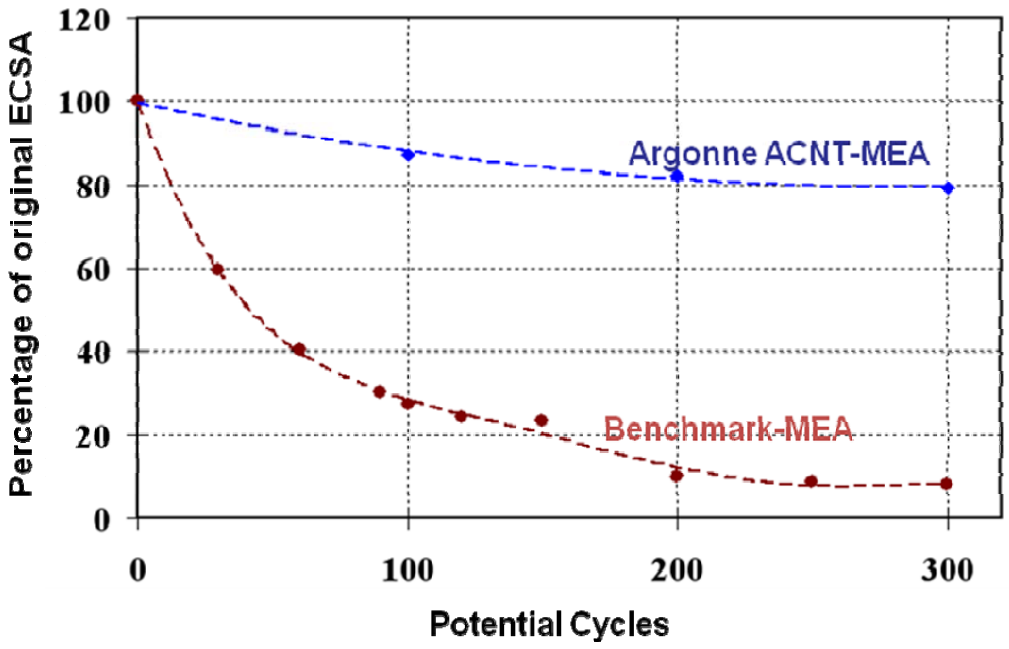

Figure 3.13. Electrochemical surface area change for ink-based and ACNT MEAs during accelerated aging test.

As the number of cycles increase, the ink-based MEA's ECSA starts decaying until it reaches 8% of its original value after 200 cycles. The ECSA for the ACNT-MEA also decreases, but it only decays to 82% of its original value after the same 200 cycles

The improved performance of ACNT-MEA compared to the ink-based MEA during the accelerated aging test can be attributed to two key factors, the Pt particle size and the carbon support stability. The initial lower value of ECSA for the ACNT-MEA suggests it has a higher average crystallite size. Larger Pt crystallites usually posses lower dissolution and re-deposition rates, therefore are capable of maintaining the surface area better than that of small Pt nanoparticles.

The platinum dispersion alone, however, could not fully account for the magnitude of changes in ECSAs, particularly in the case of ink-based MEA. Oxidative carbon corrosion, which is accelerated under high polarization potentials, can be the second major cause [8]. Carbon black usually has partially oxidized terminal groups such as –C=O, -COH, at the edge of the crystallite, which are likely to be further oxidized to CO_2 at potentials greater than 1.2 V. The oxidation will lead to the shrinkage of the CB particle size and deterioration of the electrical connection between particles. To verify this, we measured the ohmic resistance (R_{ohm}) of both MEAs, before and after the potential cycling, using AC impedance. The R_{ohm} increases 40% after 300 cycles (from 13.015 mΩ to 18.273 mΩ) for the ink-based MEA and only 0.7% for the ACNT-MEA

(from 17.737 mΩ to 17.863 mΩ). The R_{ohm} is the combination of the protonic and electronic resistances from the electrodes, electrolyte and electric contacts in the cell. Taking in account that the same Nafion® membrane and fuel cell hardware were used, the changes of the R_{ohm} are primarily from the electrodes. The oxidative corrosion can also result in the destruction of the porous structure and the blockage of gas passage in CB based electrode causing the mass transport loss in addition to increase of resistance [9]. The small increment in R_{ohm} for the ACNT-based MEA validates its design hypothesis that the graphitic nanotubes are more resistant to corrosion than CB and the nano-architecture of the vertical alignment maintains uninterrupted electronic conduction along the nanotubes [10].

3.5. Conclusions

The preliminary results obtained in this investigation have shown that the ACNT-MEA presents improved power density at the high current region when compared to a conventional ink-based MEA; proving that better mass transport can be achieved, as well as enhanced thermal and electrical conductivity, due to the unique architecture of the ACNTs.

It has also been demonstrated through ECSA and AC impedance measurements that the ACNT-MEA posses higher stability under the corrosive environment of

the FC, due to the strong corrosion resistance of the CNTs and bigger Pt particles size resulting from the wet chemistry catalysis method.

Additional results have shown evidence of a strong dependence of the ACNT-MEA performance on the ACNTs length and the amount of Nafion ionomer used. The optimum values for these parameters to accomplish further improvement the ACNT-MEA performance has yet to be found. In addition, optimization of the ACNTs structure and catalyst dispersion method can lead to further reduction of the amount of Pt used in the FC.

4. Electrochemical Studies of Non-Precious Group Metal Catalysts for PEMFC Cathode Applications

4.1. Introduction

An ideal PEMFC cathode catalyst material should be able to reduce oxygen directly to water at a high potential, be stable under the corrosive and acidic conditions of the FC, to be cheap and abundant. These characteristics pose a great challenge for non-precious group metal (non-PGM) catalyst, especially when compared in performance to Pt. The onset oxygen reduction reaction (ORR) potential of Pt catalyst is around 0.9 V, and Pt can reduce oxygen directly to water via the 4 electrons transfer mechanism; as a novel metal, Pt also presents high stability in the FC environment.

One of the most important requirements for a good non-PGM ORR catalyst material is the ability to reduce oxygen directly to water via the 4-electron transfer mechanism, according to equation (4.1).

$$4H^+ + O_2 + 4e^- \rightarrow 2H_2O \qquad (4.1)$$

Half reduction of oxygen via 2-electron transfer process, as shown by the reaction on equation (4.2), generates H_2O_2, which is detrimental for the Nafion® membrane electrolyte, not to mention the energy loss due to incomplete conversion of oxygen to water.

$$2H^+ + O_2 + 2e^- \rightarrow H_2O_2 \qquad (4.2)$$

The work described in this chapter was done at Argonne National Laboratory, who owns the copyrights. It is based on the papers: "Porous Cobalt-containing Polymer as New Electrode Catalyst for Oxygen Reduction Reaction". G. Goenaga, S. Yuan, A. Call, L. Liu and D.J. Liu. In preparation. "Cobalt Imidazolate Framework as Precursor for Oxygen Reduction Reaction Electrocatalyst". S. Ma, G. Goenaga, A. Call, D.J. Liu. In preparation.

The RRDE experiment allows one to calculate the number of electrons transferred, n, via a relationship between the disk current (I_d) and the ring current (I_r) as described by equation (4.3):

$$n = \frac{4I_d}{I_d + I_r/N} \qquad (4.3)$$

Where N is the collection efficiency, a measurement of how much of the product of the reaction on the disk electrode can be detected by the ring electrode.

Since the discovery of ORR activity of Cobalt phthalocyanine [1], extensive investigation have been done in N_4-M or N_2-M (M = Fe or Co) macromolecular precursors for preparation of non-PGM catalysts. When these precursors are absorbed/impregnated in a carbon support and pyrolyzed at high temperatures (>500 ^oC) in the presence of a nitrogen source, such as NH_3, they become catalytically active towards ORR activity [2-8]. It has been established that these types of materials become catalytically active when nitrogen, metal and carbon are present simultaneously. If only metal and carbon, or nitrogen and carbon are present, the material is inactive [2, 4-7]. Also has been discovered that at high (>800 ^oC) pyrolysis temperatures, ORR potential decreases but the stability of the material increases [5-8]. It has been proposed that the active sites for ORR have the composition N_4MC_x or N_2MC_y, depending on the type of transition metal used [2, 3, 9, 10]. More recently attention has been focused on metal supported by polymers, or polymer-carbon composites with or without pyrolysis treatment. For instance, Bashyam and Zelenay found ORR activity on a Cobalt polymer

composite, with catalytic sites composed of Co ligated to pyrrolic nitrogen [5]. When a similar non-PGM polymer composite is pyrolyzed under an inert atmosphere, improved catalytic activity is accomplished [6]. Lefèvre et al. demonstrated a significant enhancement in ORR activity in carbon-supported iron-based catalysts and suggested that micropores (width < 20 Å) have critical influence on the formation of active sites with the cations coordinated by pyridinic nitrogens [10].

These previous studies have pointed out the importance of N_4-M entities, either serving as the precursors or as the active centers for the ORR process, and have focused on the introduction of nitrogen sites to the porous carbon supports by post treatment or post impregnation of nitrogen containing ligand molecules. However, very few authors have reported the formation of active nitrogen coordinated metal sites directly.

To compensate for low catalytic activity of non-PGM compared to Pt, without affecting mass transport by excess use of the catalyst, it is desirable to produce the highest possible active site density accessible to gas diffusion through a porous framework inside of the catalyst. Herein, we report two new types of materials with active catalytic sites created through concerted approaches: In the first one, cobalt complexes were coordinated with the built-in pyridinic ligands of a porous conjugated polymer during the polymerization reaction; the second is a Cobalt-based porous metal organic framework (MOF). Electrochemical

characterization of the ORR activity of these materials after various treatments will be discussed.

4.2. Experimental

The materials were characterized using several different techniques. Brunauer-Emmett-Teller (BET) experiments were used to determine the surface area and pore size distribution in the fresh materials and after heat treatments. SEM, TEM, X-ray Photoelectron Spectroscopy (XPS) and elemental analysis were used to determine morphology and chemical composition. The electrochemical characterization and durability were carried out using RDE and RRDE experiments.

To determine the effect of temperature on the electrochemical performance of these materials, samples were heat treated at temperatures ranging between 500 and 900 ^{o}C. In general, 15 mg of the sample were weighed in a ceramic boat and placed in a 1" diameter quartz tube. The tube was air sealed and placed inside a furnace at the desired temperature for 1 hour, in an Argon gas atmosphere at a flow rate of 100 mL/min. The yield after the heat treatment is normally between 40 and 60%, depending on the temperature. The sample obtained after heat treatment was used to prepare an ink for the electrochemical characterization experiments. The ink containing the Co-based electrocatalysts was prepared using a 3:7 Nafion ionomer to Catalyst ratio, dissolved in 5 wt%

Nafion® ionomer and methanol. The solution obtained was magnetically stirred for at least a week before testing.

The ORR activity and electron transfer mechanism of both catalysts were studied using RDE and RRDE experiments. The electrolyte used was 0.1 M Perchloric acid ($HClO_4$), contained in a three compartment glass cell. The reference electrode was an Hg/Hg_2SO_4 electrode, filled with 0.5 M sulfuric acid (H_2SO_4) solution, and a gold wire was used as the counter electrode. The working electrode used was the Pine Instruments model AFE7R9GCAU, with a glassy carbon (GC) disk and a gold ring. The GC carbon disk had a diameter of 5.61 mm and the inner and outer diameters of the Au ring were 6.25 and 7.92 respectively, with 37% collection efficiency. The disk potential was controlled with the electrochemical work station 760C from CH Instruments that uses the software CHI760 for the data acquisition. The rotation rate of the electrode was controlled with the MSRX speed controller from Pine instruments. Prior to the ink deposition, the GC disk was polished with 0.05 micron Gamma Micropolish alumina powder and rinsed generously with high purity DI water. For each experiment, 20 to 30μL of the ink were pipetted on to the GC electrode, targeting a dry weight of between 150 and 200 μg, or the equivalent of 600 to 800 $\mu g/cm^2$. The ink was dried at room temperature until the solvents evaporated completely leaving a mixture of Nafion® and catalyst deposited on the GC disk. The experiments were conducted at room temperature, under ultra high purity Argon and Oxygen gases, at rotation speeds between 625 and 2500 rpm. The $HClO_4$

electrolyte was purged on each gas for at least 30 minutes and during the experiments gas flow was maintained over the solution. The voltammograms collected under argon were subtracted from the ones collected under oxygen to obtain the background corrected ORR polarization graphs.

4.3. Porous Cobalt-containing polymer catalyst

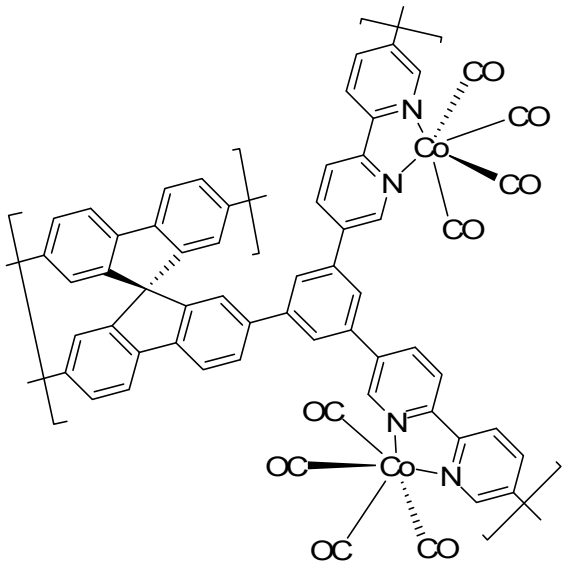

Figure 4.1. Proposed structure for Co-PBPY. Co metal is coordinated with two N atoms.

This is a porous conjugated polymer containing coordinated cobalt complexes (Co-PBPY). It was prepared through copolymerization of ethynyl functionized spirobifluorene and bipyridine (in 1 to 2 ratio) catalyzed by excess amount of $Co_2(CO)_8$. The stereo-contorted spirobifluorene helps maintain the porous structure in the resulted polymer, and the bipyridine provides nitrogen coordination ligands for the cobalt complex. $Co_2(CO)_8$ acts as both complexation

metal source and catalyst for the trimerization reaction of ethynyl functional groups. Figure 4.1. shows the proposed structure of the material as synthesized.

The fresh sample does not present electrocatalytic activity towards ORR; however, the activity is greatly enhanced after heat treatment at high temperature. The Co-PBPY was heat treated at temperatures ranging between 500 and 900 ^{o}C. Cyclic voltammograms in argon and oxygen gases were recorded at a rotation speed of 1600 rpm and a scan rate of 10 mV/s. The argon background is subtracted from the oxygen polarization curves, and the corrected current densities are plotted vs. standard hydrogen electrode (SHE) potential. Figure 4.2. shows the impact of the temperature on the ORR activity of the Co-PBPY material. The onset potential increases as the treatment temperature increases, reaching a maximum at 700 ^{o}C, and decreasing at higher temperatures. The sample pyrolyzed at 500 ^{o}C shows little ORR activity, which can be attributed to incomplete carbonization of the polymer, resulting in both, poor electronic conductivity and very few active catalytic sites exposed to the reactant gas. Upon heat treatment at 600 ^{o}C, the material starts showing ORR activity; with the onset potential reaching a maximum value of 0.78 V for the sample treated at 700 ^{o}C; while higher temperature treatment was found to be detrimental to the ORR catalytic performance. The BET surface area of the fresh sample was around 210 m^2/g, and increased to around 550 m^2/g after pyrolysis at 700 ^{o}C, which is an indication that the micro porosity of the polymer was maintained during pyrolysis process at the same time that new porosity was

created. As a consequence, more active catalytic sites are exposed to take part in the ORR, and increased catalytic activity is observed. At temperatures above 700 ^{o}C the carbon support starts to become graphitized, encapsulating the Co metal particles and preventing them from taking part in the ORR.

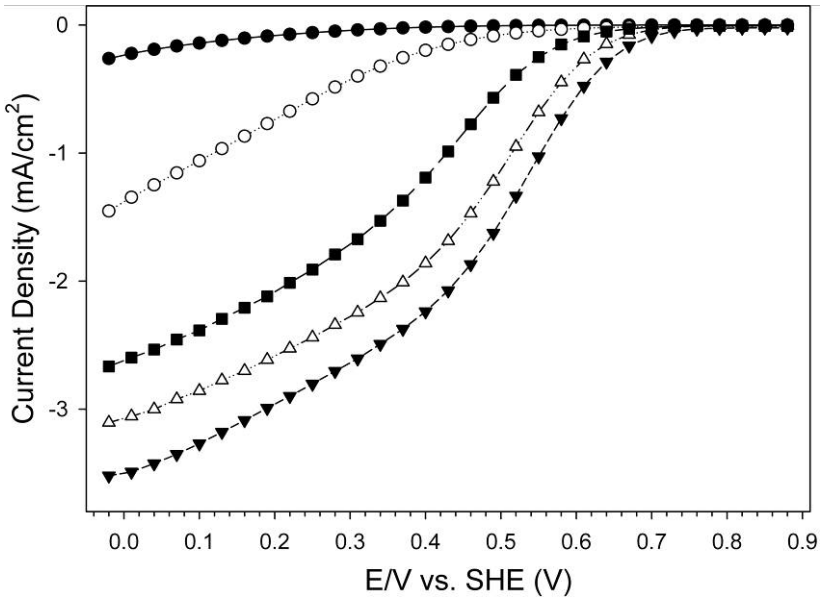

Figure 4.2. Effect of thermal treatment on ORR activity of Co-PBPY. Co-PBPY treated at 500 ^{o}C, solid circle; 600 ^{o}C, hollow circle; 700 ^{o}C, solid triangle; 800 ^{o}C, hollow triangle; and 900 ^{o}C, solid square. Rotating speed = 1600 rpm, catalyst loading = 800 µg/cm^2.

As expected, the temperature treatment also has a great impact on the number of electrons transferred during the ORR. Figure 4.3. shows that for temperature treatment above 700 ^{o}C, the Co-PBPY reduces oxygen directly to water via 4-electron transfer mechanism in the potential range from 0 V to 0.8 V, which is in good agreement with what was observed in Co-TPPS (tetrakis-sulfophenyl-porphine) by Zhou et al [4] and Co-PANI (polyaniline) by Wu et al [6].

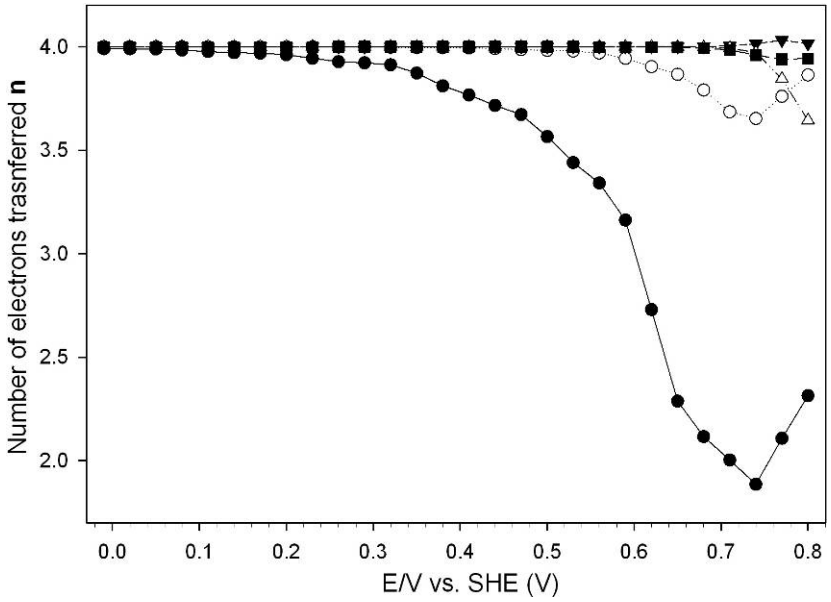

Figure. 4.3. Electron transfer mechanism for Co-PBPY. Co-PBPY treated at 500 ^{o}C, solid circles; 600 ^{o}C, hollow circles; 700 ^{o}C, solid triangles; 800 ^{o}C, hollow triangles; 900 ^{o}C, solid squares.

Optimization of the polymerization conditions by extended sonication of the reaction mixture before refluxing led to a sample with slightly higher overall surface area, and the catalyst prepared from this new batch of Co-PBPY shows slightly improved mass transfer. This new sample was used for all the measurements shown hereafter.

The Co content in Co-PBPY sample was relatively high, as can be expected from the synthesis procedure. Elemental analysis revealed that the Co content in the as synthesized sample was about 10% by mass and that it increased to 20% after the sample was pyrolyzed at 700 ^{o}C. Since the yield of pyrolysis under experimental conditions is about 50%, this result confirms no Co was lost during the heat treatment. Previous studies by Dodelet's group showed that increasing

the material's metal content can improve the ORR activity, though a saturation point is quickly reached, after which increasing the amount of metal yields no improvement effect on the performance, and for some materials even decreases the catalytic activity [10]. To reduce the Co content in the Co-PBPY sample, it was acid leached with concentrated HCl. Elemental analysis showed the Co content is reduced to about 1.2% before and 1.7% after pyrolysis at 700 ^{o}C. Figure 4.4. compares the ORR activity of the Co-PBPY before and after acid treatment, after both samples have been pyrolyzed at 700 ^{o}C. As can be observed, there is no significant difference in the catalytic performance despite the Co content difference, which indicates that at 1.7% metal content the sample is already at its saturation point.

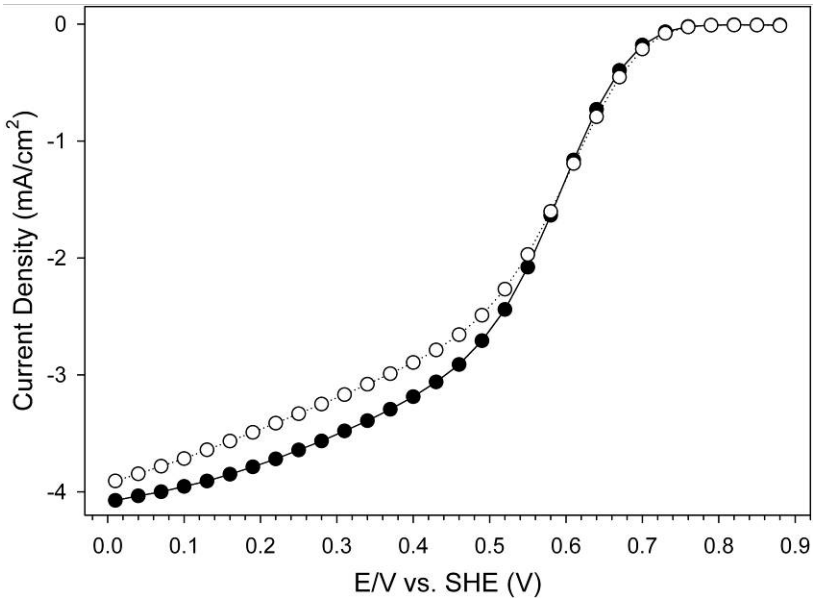

Figure 4.4. Effect of metal content on ORR activity for Co-PBPY. Co-PBPY treated at 700 ^{o}C with cobalt content of 20%, solid circles and 1.7%, hollow circles.

After the Co-PBPY is pyrolyzed, additional chemical treatment can lead to improved catalytic activity. For example, electrocatalytic improvement was observed when the Co-PBPY, heat treated at 700 ^{o}C, was acid leached in 0.5 M H_2SO_4. The acid leach can wash the excess metal away, exposing hidden catalytic sites to the ORR reaction. It also helps to sulfonate and/or oxidize the carbon support, making it more compatible with the Nafion ionomer. Figure 4.5. shows that acid leaching improves Co-PBPY mass transfer properties.

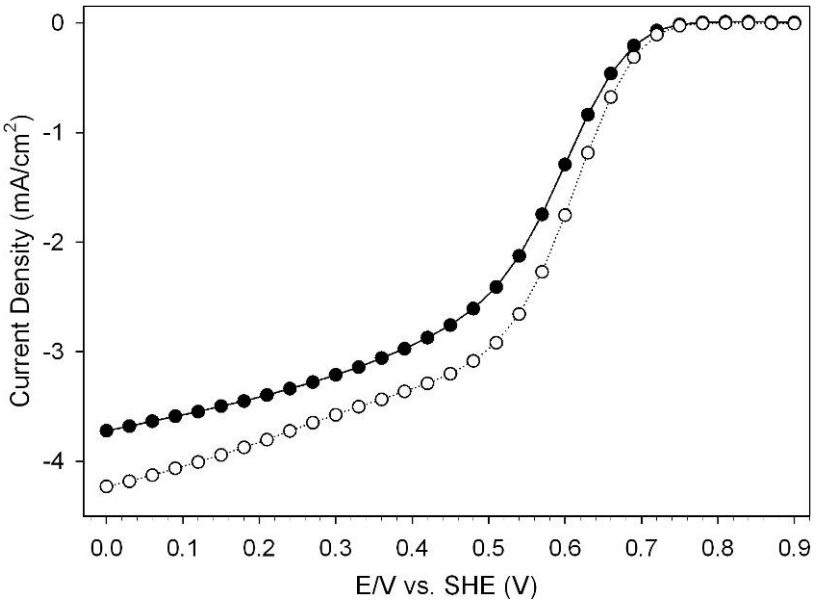

Figure 4.5. Effect of 0.5 M H_2SO_4 acid treatment on ORR activity of Co-PBPY. Co-PBPY at 700 ^{o}C before acid treatment, solid circles, and after acid treatment, hollow circles.

On the other hand, introducing pyridinic or pyrolic nitrogen to the sample can form additional catalytic sites when the nitrogen coordinates to excess cobalt complexes. The pyridinic or pyrolic nitrogen can be added by impregnating a N-containing compound, such as imidazole or cyanamide, into the fresh sample (as

prepared Co-PBPY polymer), or by heat treating the sample with NH_3 as the carrier gas after an initial heat treatment under Ar. Both processes of introducing nitrogen to the sample show certain increase on the ORR onset potential. Figure 4.6. shows the effect of adding imidazole and cyanamide before heat treatment.

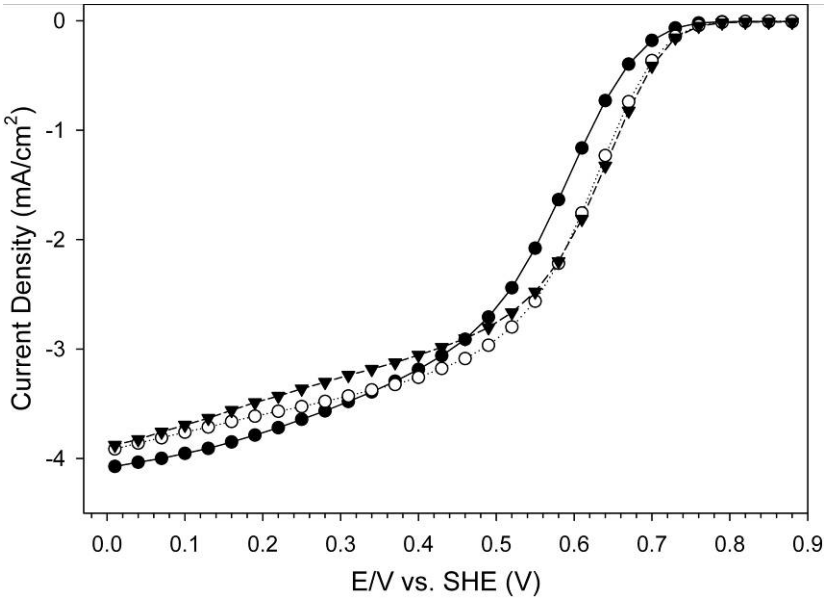

Figure 4.6. Co-PBPY with solvent added previous heat treatment. Co-PBPY at 700 ^oC, solid circles; Co-PBPY/cyanamide treated at 700 ^oC, hollow circles; and Co-PBPY/imidazole treated at 700 ^oC, solid triangles.

In the case of post heat treatment under NH_3, the mass transfer was also improved, reaching the highest current density of about 4.7 mA/cm^2 among the various chemical treatments performed on Co-PBPY sample. Figure 4.7. shows the ORR activity for a Co-PBPY sample that was heat treated a 700 ^oC under Argon followed by another heat treatment under NH_3 at 600 ^oC for one hour.

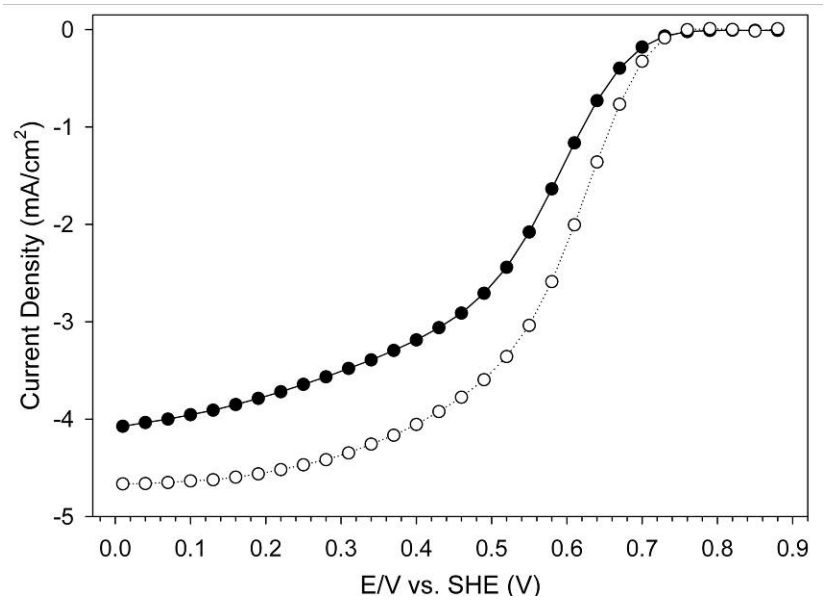

Figure 4.7. Co-PBPY post treated with NH_3. ORR activity for Co-PBPY treated at 700 ^oC under Ar only, solid circles; followed by a second treatment under NH_3 at 600 ^oC, hollow circles.

4.4. Cobalt Imidazolate Framework Catalyst

In this thesis, for the first time, the use of porous metal organic frameworks (MOFs) for catalytic ORR application is investigated. M-N_4 entities can be grafted into MOFs with very high volumetric density, and be regularly arranged on their pore walls [11] directly accessible by the gas reactants through the network of the porous channels. The pore sizes of MOFs are typically less than 20 Å and are tunable via controlling the length of linkers. Furthermore, the metal-ligand composition can be altered through rational design and the high crystallinity of the ordered structure enables the catalytic active sites formed to be uniformly distributed throughout the hydrocarbon matrix.

The cobalt imidazolate (Co-I) frameworks were selected as potential candidates for ORR catalysts, because in these structures each cobalt atom is coordinated with four nitrogen atoms of imidazolate ligands (Figure 4.8.) and the CoN_4 moieties are all regularly dispersed in their frameworks. Under solvothermal conditions, the reaction between the 3,5-imidazolate and $Co(NO_3)_2 \cdot 6H_2O$ in N,N′-dimethylacetamide (DMA) afforded some purple crystals of the cobalt imidazolate framework. In Co-I, every cobalt atom binds four nitrogen atoms from four 3,5-imidazolate ligands and each 3,5-imidazolate ligand connects with two cobalt atoms to form a three-dimensional porous structure with pore size of ~4 Å along the [1 0 0] direction (Figure 4.8 b). The number of CoN_4 moieties in the single crystal of Co-I can reach as high as $3.6 \times 10^{21}/cm^3$ (based on the crystal density of 1.162 g/cm^3). BET surface area of Co-I is 305 m^2/g, indicating the porosity of the material.

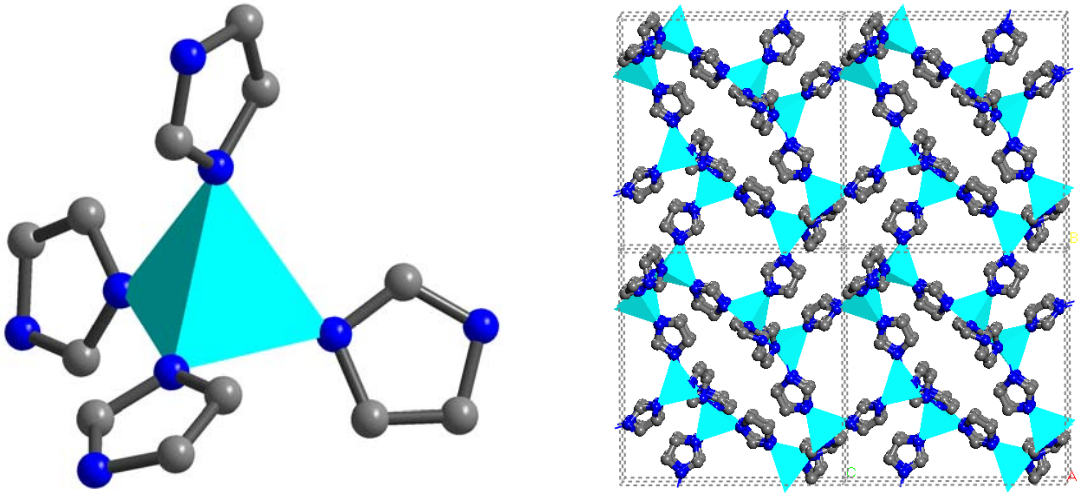

(a) (b)

Figure 4.8. Co-I structure. (a) Local CoN_4 coordination moiety; (b) Structure-packing of Co-I along the [1 0 0] direction (color scheme: turquoise, Co; Blue, N; Grey, C).

The electrochemical properties of Co-I were also studied using RDE and RRDE experiments. The fresh sample showed little ORR activity, which can be attributed to the insulating nature of the Co-I framework. However, the ORR activity, can be substantially enhanced when the sample is heat treated at different temperatures under Ar atmosphere, as is shown by Figure 4.9. The Co-I started to demonstrate ORR activity after it was heated at 600 ^{o}C, presenting an onset potential of 0.76 V. An optimal performance was achieved for the sample pyrolyzed at 750 ^{o}C with an onset potential of 0.81 V, which is higher than those of cobalt porphyrins supported on activated carbons and carbon nanotubes [12]. Further increase of the pyrolysis temperature decreases ORR activity. The I-V polarization curve also shows a rapid increase of the current density as the function of voltage, reaching a limiting current for treatment temperatures above 700 ^{o}C.

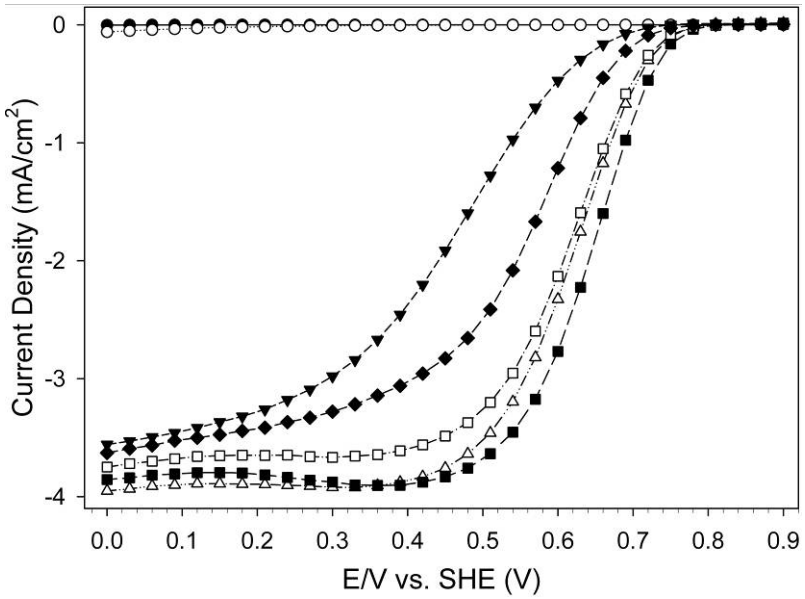

Figure 4.9. Effect of temperature treatment on Co-I ORR activity. Co-I fresh sample, solid circles; 500 ^{o}C, hollow circles; 600 ^{o}C, solid triangle; 700 ^{o}C, hollow triangle; 750 ^{o}C, solid square; 800 ^{o}C, hollow square; 900 ^{o}C, solid diamond. Rotating speed = 1600 rpm, catalyst loading = 600 μg/cm^2

The sample calcined at 750 ^{o}C, with the best ORR activity, has a BET surface area of 255 m^2/g, preserving more than 80 percent of the initial pore volume and surface area. The limiting current indicates that all of the oxygen reaching the catalyst on the GC disk is being reduced.

The electron transfer mechanism was determined by RRDE, resulting in n = 4 for temperature treatments above 600 ^{o}C, as shown in figure 4.10. This indicates that Co-I reduces oxygen directly to water.

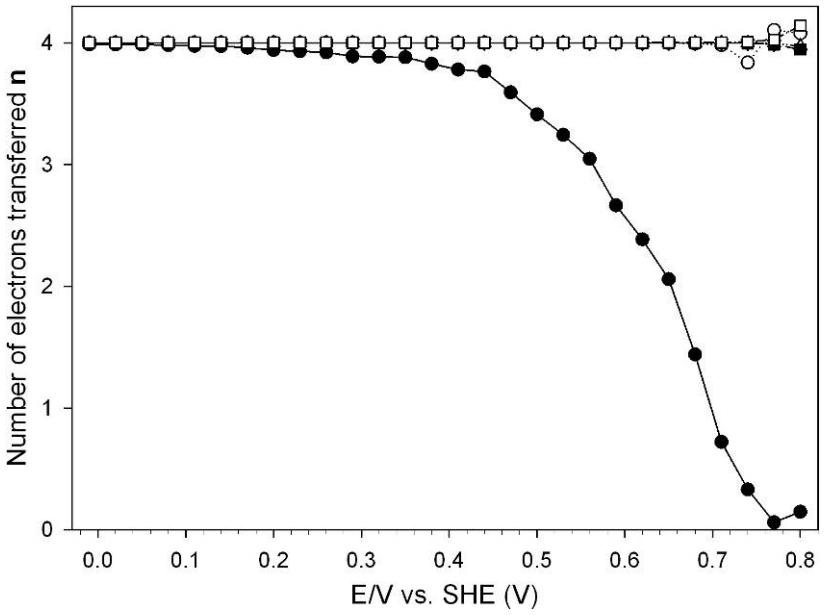

Figure 4.10. Number of electrons transferred for Co-I treated at different temperatures. Co-I fresh sample, solid circles; 500 ^{o}C, hollow circles; 600 ^{o}C, solid triangle; 700 ^{o}C, hollow triangle; 750 ^{o}C, solid square; 800 ^{o}C, hollow square; 900 ^{o}C, solid diamond.

Chemical post treatment with NH_3 and H_2SO_4 was also explored for Co-I, however, the improvement was not as significant as for Co-PBPY. Figure 4.11. shows a comparison of Co-I treated at 750 ^{o}C and the same sample after acid

leaching with H_2SO_4. The onset potential and mass transfer in both cases is virtually the same, but acid treatment can improve the stability of the sample. The Co-I sample was acid treated with H_2SO_4, followed by a second heat treatment at 750 ^oC.

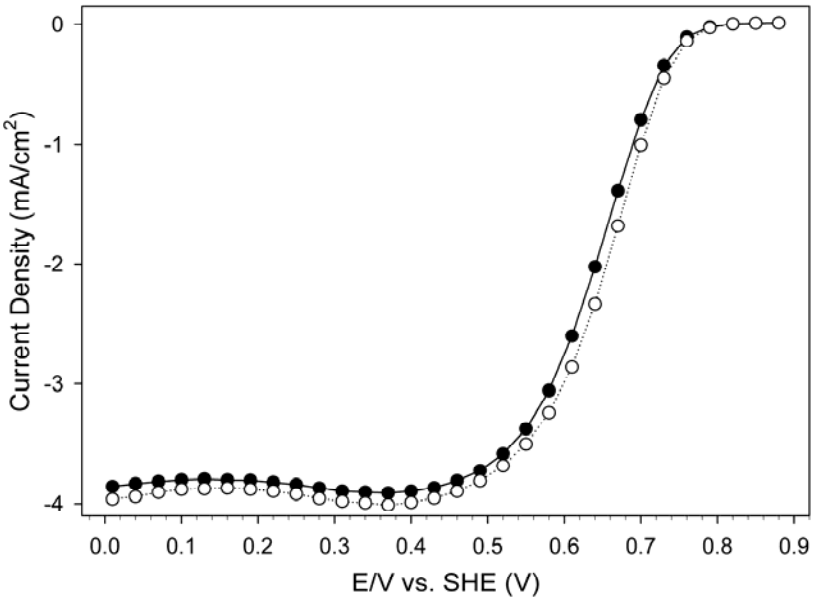

Figure 4.11. Effect of 0.5 M H_2SO_4 acid treatment on ORR activity of Co-I. Co-I treated at 750 ^oC, solid circles; Co-I treated at 750 ^oC and acid leached, hollow circles.

Chronoamperometry experiments were carried out in both samples for three hours. In this experiment voltage was switched between 0.35 V and 0.7 V vs. SHE, while current was measured. Figure 4.12. shows that the acid treated sample presents higher stability over the 3 hours experiment duration. The metal content in the fresh Co-I is about 30%. Excess metal can get dissolved during operation conditions, causing catalyst degradation. Acid treatment washes away the excess metal, and the second heat treatment helps to reorganize the catalytic sites in the pore channels, giving more stability to the

material. Acid treatment also improves the ink dispersion on the GC electrode, avoiding catalyst separation from the electrode.

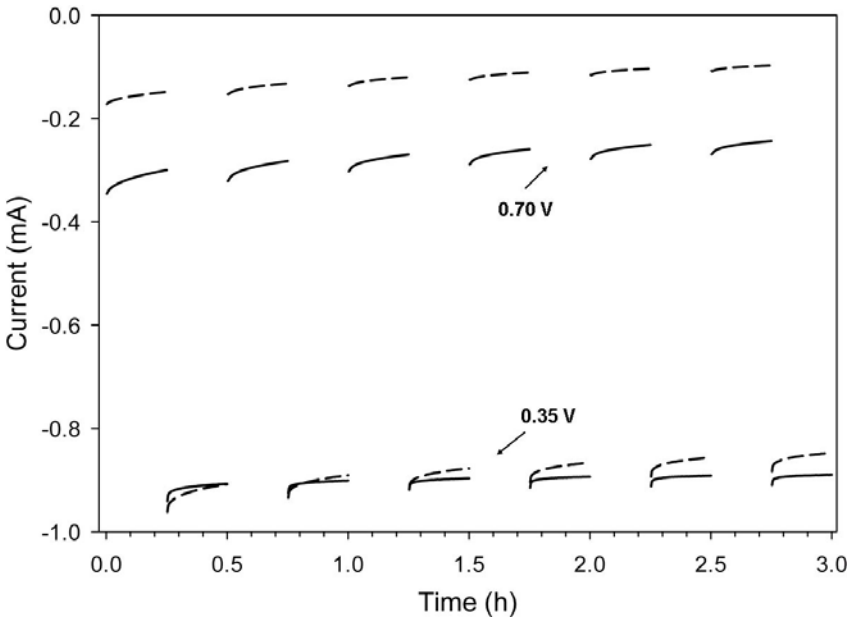

Figure 4.12. Chronoamperometry experiments for durability of Co-I. Co-I 750 ^{o}C, dash line; Co-I 750 ^{o}C acid leached, solid line.

4.5. Conclusions

Two novel approaches in the synthesis of ORR electrocatalyst precursors have been demonstrated. Both materials, the cobalt containing porous polymer and the porous cobalt imidazolate framework, can be converted into active materials, with catalytic activity towards ORR, with a simple heat treatment under Argon inert atmosphere. The active catalytic sites in both cases are believed to be formed by Co fully coordinated with nitrogen.

Preliminary results show that the onset potential and mass transfer characteristics of both materials, at the optimum treatment temperature, are comparable to other state of the art Co based electrocatalysts. Chemical treatment after the initial pyrolysis has shown further improvement in the catalytic activity.

The versatility of both materials is based in the high density of active sites, and their capability of being used as templates for different metal o metal alloys centers. Co can be replaced or combined with Fe, Ta, Ni in other materials. In addition, the pore size in both materials can be designed and controlled using different starting monomers or ligands.

It is important to highlight that this is the first time a MOF was used as an ORR catalyst. The richness of the MOFs field offers a complete new route to different types of ORR electrocatalytic precursors.

5. Conclusions

Nafion composite membranes prepared by introducing hydrophilic inorganic metal particles (TiO_2, SiO_2 and $Zr(HPO_4)_2$ to Nafion membranes, were studied using the NMR technique. In general, fully hydrated (with water or 2M methanol solvent) Nafion composite membranes present higher solvent uptake and higher solvent retention, when compared to filler free Nafion.

NMR self diffusion measurements show that most of the composite membranes present higher water mobility than the pure Nafion membrane. The $Zr(HPO_4)_2$ composite membrane, prepared ex-situ, also presented lower methanol diffusivity than Nafion, what translates in an improved methanol crossover characteristic. High pressure NMR self-diffusion measurements in the $Zr(HPO_4)_2$ composite membrane hydrated at 20%, reveals lower activation volume for the composite membrane, and indication of improved water transport due to the modification of the Nafion-composite polymer channel structure.

The use of ACNTs as Pt catalyst support in PEMFC cathode was studied. The unique architecture of the ACNTs allows a uniform Pt nanoparticles distribution along the nanotubes walls and, in addition provides a straight path for the reactant gases to reach the ORR catalytic sites. The alignment, along with the hydrophobicity of the NTs improved the water management in the FC cathode, reducing losses caused by flooding issues. All these factors contribute to

enhanced mass transport properties of the ACNTs MEA when compared to a Pt catalyst supported in CB MEA. Moreover, the high corrosion resistance, mechanical stability and electron conductivity of the ACNTs contribute to improve the durability of the PEMFC. The improvement was accomplished while reducing the amount of Pt catalyst used, compared to a CB Pt supported commercial MEA.

Two novel non-PGM catalysts were investigated, a Co containing porous conjugated polymer and Co imidazolate MOF. The as synthesized materials were inactive catalysts for ORR, however, heat treatment at high temperatures under inert atmosphere, promotes their ORR catalytic activity. In both materials, it is believed the active centers are formed by Co coordinated with nitrogen.

Chemical treatment after the initial heat treatment can help to improve the onse potential mass transport of the materials. For instance, acid treatment with H_2SO_4 helps to sulfonate/oxidize the carbon support while washing away the excess metal in the sample, leading to better ink dispersion and higher stability. In the case of Co-PBPY, introducing nitrogen, previous or post pyrolysis can help to create new active catalytic sites, improving the onset potential and mass transfer. The effect of combining both chemical treatments still needs to be studied.

The 3-D structure of these materials can be used a template for creating new metal centers, replacing or combining Co with other transition metals, such as Fe, Ni or Ta. The pore size of both materials can be designed and controlled using different starting monomers or ligands.

6. Bibliography

Chapter 1

[1]. A.J. Appleby, F.R. Foulkes. *Fuel Cell Handbook*. Krieger Publishing Company, Malabar, FL. (1993).

[2]. M. H. Levitt, Spin dynamics. *Basics of nuclear magnetic resonance.* John Wiley and Sons, ltd. March 2005.

[3]. H. Friebolin, *Basic one- and two-dimensional NMR spectroscopy*. Wiley-VCH. 2005.

[4]. E. Fukushima, S. Roeder. *Experimental Pulse NMR*. *A nuts and bolts approach.* Addison Wesley Inc. (1981).

[5]. C. S. Johnson, Jr. *Diffusion Measurements by magnetic field gradient methods*. Encyclopedia of NMR, Wiley, New York, 1626-1644 (1995).

[6]. *Probing Fuel Cell Electrocatalyst Properties Using Pine Rotating Disk and Ring-Disk Electrodes* Technical Note 2005-01 Pine research instrumentation.

[7]. A.J. Bard and L.R. Faulkner, *Electrochemical Methods-Fundamentals and Applications, 2nd Edition*, John Wiley & Sons, New York (2000).

[8]. R. Wang, S. Liao_, H. Liu and H. Menga. *Journal of Power Sources*, 2007 **171**, 471.

[9]. E. Claude, T. Addou, J.M. Latour, P. Aldebert. *Journal of applied electrochemistry*, 1998, **28**, 57.

[10]. S. Marcotte, D. Villers, N. Guillet, L. Roue, J.P. Dodelet. *Electrochimica Acta*, 2004, **50**, 179.

[11]. F. Barbir. *PEM Fuel Cells. Theory and Practice*. Elsevier Academic press. London (2005).

[12]. J. Larminie, A. Dicks. *Fuel Cell Systems Explained*. 2nd Edition. John Wiley & Sons, West Sussex (2003).

Chapter 2

[1]. K.T. Adjemian, S. Srinivasan, J. Benziger, A.B. Bocarsly, *Journal of Power Sources,* 2002, **109,** 356.

[2]. Adjemian KT, Lee SJ, Srinivasan S, Benziger J, Bocarsly A.B., *Journal of Electrochemical Society,* 2002, **149**, A256.

[3]. A.S. Arico, P. Creti, P.L. Antonucci, V. Antonucci, *Electrochemistry and Solid-State Letters*, 1998, **1**, 66.

[4]. K.D. Kreuer, *J. Membr. Sci.*, 2001, **185**, 29.

[5]. P. Staiti, A.S. Arico, V. Baglio, F. Lufrano, E. Passalacqua, P.L. Antonucci, *Solid State Ionics*, 2001, **145**, 101.

[6]. P. Costamagna, C. Yang, A.B. Bocarsly, S. Srinivasan, *Electrochim Acta*, 2002 **47**, 1023.

[7]. D.J. Jones, J. Roziere. In: Vielstich Lamm Gasteiger WAH (ed) Handbook of fuel cells, fundamentals, technology and applications. Wiley, London, 2003, p. 447.

[8]. P. Dimitrova, K.A. Friedrich, B. Vogt, U. Stimming, *J. Electroanal. Chem*. 2002, **532**, 75.

[9]. A.S. Arico, V. Baglio, V. Antonucci, I. Nicotera, C. Oliviero, L. Coppola, P.L. Antonucci, *J Membr Sci*., 2006, **270**, 221.

[10]. H.A. Every, T.A. Zawodzinski. In: Meeting AS (ed) Fuel cell technol.: membr. New Orleans, 2002, p 558.

[11]. E.O. Stejskal, J.E. Tanner, *J. Chem. Phys.*, 1965, **42**, 288.

[12]. J.J. Fontanella, C.D. Edmonson, M.C. Wintersgill, Y. Wu, S.G. Greenbaum *Macromolecules*, 1996, 29, 4944.

[13]. J.J. Fontanella, M.C. Wintersgill, R.S. Chen, Y. Wu, S.G. Greenbaum Electrochem Acta, 1995, **40**, 2321.

[14]. J.P.R. Jayakody, P.E. Stallworth, E.S. Mananga, J.F. Zapata, S.G. Greenbaum, J Phys Chem B , 2004, **108**, 4260.

[15]. I. Nicotera, T. Zhang, A.B. Bocarsly, S.G. Greenbaum, Journal of Electrochemical Society, 2007, **154**, B466.

[16]. C. Yang, S. Srinivasan, A.B. Bocarsly, S. Tulyani, J.B. Benziger, *J Membr Sci*, 2004, **237**, 145.

[17]. M. H. Levitt, Spin dynamics. Basics of nuclear magnetic resonance. John Wiley and sons, ltd., 2005.

[18]. R.H. Yoon, S. Vivek. *J Colloid and Interface Sci*, 1998, **204,**179.

[19]. M. Holz, S.R. Heil, A. Sacco. *Phys Chem Chem Phys*, 2000, **2**, 4740

Chapter 3

[1]. M. S. Wilson and S. Gottesfeld, *J. of Appl. Electrochem,* 1992, **22**, 1.

[2]. J. Appleby, F.R. Foulkes, Fuel Cell Handbook. 1993. Krieger Publishing Company.

[3]. R. J. Mashl, S. Joseph, N. R. Aluru and E. Jakobsson, *Nanotech,* 2003, **1**, 152.

[4]. D. J. Mann and M. D. Halls, *Phys. Rev. Lett*., 2003, **90**, 195503.

[5]. Z.-B. Wang, G.-P. Yin and P.-F. Shi, *Carbon*, 2006, **44**, 133.

[6]. United states Fuel cell Council, single cell test protocol, US FCC 05-014 and 2006.

[7]. R. Makharia, S. Kocha, P. T. Yu, M. A. Sweikart, W. Gu, F. T. Wagner, H. A. Gasteiger, *ECS Transactions,* 2006, **1**, 3.

[8]. Cao, P. L. Dickrell, W. G. Sawyer, M. N. Ghasemi-Nejhad and P. M. Ajayan, Science, 2005, 310, 1307.

[9]. V. Zaporotskova and N. G. Lebedev, The research of the mechanism of proton conductivity in single-walled carbon nanotubes, in *6th Biennial International Workshop on Fullerenes and Atomic Clusters, IWFAC 2003*, St. Petersburg, Russia.

[10]. J. Yang, G. Goenaga, A. Call, D.J. Liu, *Electrochemical and Solid-State Letters.* 2010, **13**, B55.

Chapter 4

[1]. Jasinski, R. *Nature*, 1964, **201**, 1212.

[2]. F. Jaouen, S. Marcotte, J.P. Dodelet and G. Lindbergh, *J. Phys. Chem. B*, 2003, **107**, 1376.

[3]. C. Medard, M. Lefevre, J.P Dodelet, F, Jaouen and G. Lindbergh, Electrochimica Acta, 2006, 51, 3202.

[4]. Q. Zhou, C. Ming Li, J. Li, X. Cui and D. Gervasio. *J. Phys. Chem. C*, 2007, **111**, 11216.

[5]. R. Bashyam and P. Zelenay, *Nature*, 2006, **443**, 63.

[6]. G. Wu, Z. Chen, K. Artyushkova, F. Garzon and P. Zelenay, *ECS Transactions*, 2008, **16**, 159.

[7]. A. Leela, N. Rajalakshmi and S. Ramaprabhu, *Carbon*, 2008, **46**, 2.

[8]. H. T. Chung, C. M. Johnston, F. H. Garzon and P. Zelenay, *ECS Transactions*, 2008, **16**, 385.

[9]. M. Lefevre, J.P. Dodelet and P. Bertrand, *J. Phys. Chem. B*, 2002, **106**, 8705.

[10]. M. Lefevre, E. Proietti, F. Jaouen and J. P. Dodelet, *Science*, 2009, **324**, 71.

[11]. Kitagawa, S.; Kitaura,, R.; Noro, S.-I. *Angew. Chem., Int. Ed.*, 2004, **43**, 2334.

[12]. *Handbook of Fuel Cells – Fundamentals, Technology & Applications.* Edited by W. Vielstich, H. Yokokawa, H. A. Gasteiger. Vol **5**: *Advances in Electocatalysis, Materials, Diagnostics & Durability*. 2009 John Wiley & Sons.